J. Fluid Mech. (1994), *vol.* 273, *pp.* 323–360

Oblique-mode breakdown and secondary instability in supersonic boundary layers

By CHAU-LYAN CHANG AND MUJEEB R. MALIK
High Technology Corporation, PO Box 7262, Hampton, VA 23666, USA

(Received 25 October 1993 and in revised form 1 March 1994)

Laminar–turbulent transition mechanisms for a supersonic boundary layer are examined by numerically solving the governing partial differential equations. It is shown that the dominant mechanism for transition at low supersonic Mach numbers is associated with the breakdown of oblique first-mode waves. The first stage in this breakdown process involves nonlinear interaction of a pair of oblique waves with equal but opposite angles resulting in the evolution of a streamwise vortex. This stage can be described by a wave–vortex triad consisting of the oblique waves and a streamwise vortex whereby the oblique waves grow linearly while nonlinear forcing results in the rapid growth of the vortex mode. In the second stage, the mutual and self-interaction of the streamwise vortex and the oblique modes results in the rapid growth of other harmonic waves and transition soon follows. Our calculations are carried all the way into the transition region which is characterized by rapid spectrum broadening, localized (unsteady) flow separation and the emergence of small-scale streamwise structures. The r.m.s. amplitude of the streamwise velocity component is found to be on the order of 4–5% at the transition onset location marked by the rise in mean wall shear. When the boundary-layer flow is initially forced with multiple (frequency) oblique modes, transition occurs earlier than for a single (frequency) pair of oblique modes. Depending upon the disturbance frequencies, the oblique mode breakdown can occur for very low initial disturbance amplitudes (on the order of 0.001% or even lower) near the lower branch. In contrast, the subharmonic secondary instability mechanism for a two-dimensional primary disturbance requires an initial amplitude on the order of about 0.5% for the primary wave. An in-depth discussion of the oblique-mode breakdown as well as the secondary instability mechanism (both subharmonic and fundamental) is given for a Mach 1.6 flat-plate boundary layer.

1. Introduction

The laminar–turbulent transition process in a low-disturbance environment consists of several stages in the evolution of disturbances. The first stage involves the internalization of free-stream disturbances into the boundary-layer flow, i.e. the receptivity process (Morkovin 1969). The dominant receptivity takes place near the leading edge of the body and disturbances do not grow until a critical region is reached. The second stage, which starts beyond the critical region, is characterized by the amplification of infinitesimal disturbances which can be described by linear stability theory. For a two-dimensional low-speed boundary layer, these instability waves are referred to as Tollmien–Schlichting (TS) and Rayleigh waves for viscous and inviscid instabilities, respectively, and Mack modes (e.g. first and second modes, etc.) for viscous/inviscid instabilities (Mack 1969) which operate at higher Mach numbers. A linear amplification process may be relevant over a wide range of Reynolds numbers

depending upon the frequency and initial amplitude of the disturbance. When sufficiently high disturbance amplitude is reached through this linear growth, the evolution enters the third stage, where nonlinear interaction and a sequence of secondary instabilities cause laminar flow to break down to turbulence.

For low-speed two-dimensional flow, two breakdown mechanisms have been identified both experimentally and theoretically. These consist of fundamental and subharmonic resonance mechanisms which lead to aligned and staggered lambda vortex structures, respectively (e.g. Klebanoff & Tidstrom 1959; Klebanoff, Tidstrom & Sargent 1962; Saric & Thomas 1984; Kachanov & Levchenko 1984). When a two-dimensional Tollmien–Schlichting wave gains sufficient amplitude, oblique modes with frequency equal to or half the frequency of the TS wave are excited which lead to the lambda vortex structure and constitute the secondary instability en route to transition. In incompressible flows, this secondary instability can take place at an initial TS amplitude of much less than 1% based on the streamwise velocity component.

Craik (1971) proposed a resonant-triad model which consists of a plane TS wave and a pair of oblique waves propagating at equal but opposite angles to the mean flow direction. Using solutions of the Orr–Sommerfeld equation, Craik was able to construct a wave triad such that the streamwise wavenumber of the oblique waves equals one-half of that of the plane TS wave and the phase velocity of all three waves is identical (resonance). He then showed that such a resonant combination leads to rapid growth of three-dimensionality, even though the oblique subharmonic waves are stable according to the Orr–Sommerfeld solutions. Experimental evidence of the subharmonic breakdown was provided by Kachanov & Levchenko (1977, 1984). They found a strong wave-triad resonance with a unique phase-locking relation between the TS and oblique waves as described by Craik's model even though the excited oblique waves were not selected according to Craik's criterion.

In Herbert's (1983, 1988) Floquet-based secondary instability theory, oblique wave amplification under parametric resonance can be computed as an eigenvalue problem for a mean flow modulated by a finite-amplitude primary TS wave. Herbert was able to reproduce the amplitude evolution of both the primary and secondary (oblique) disturbances measured in Kachanov and Levchenko's experiment. The secondary instability theory of Herbert can be applied to both fundamental and subharmonic mechanisms and to any set of oblique disturbances in contrast with Craik's model where a unique phase relation between the TS oblique waves must exist according to the Orr–Sommerfeld equation.

The experiment of Saric & Thomas (1984) was performed by using vibrating ribbons to introduce both primary (two-dimensional) and secondary (three-dimensional) disturbances. Corke & Mangano (1989) used heating wires to generate the desired disturbances and performed detailed measurement of the disturbance field. They showed that Craik's resonant model is not necessary for the description of subharmonic breakdown and further verified the results of Herbert's secondary instability theory. In both experiments, smoke-wire flow visualization demonstrates a staggered peak–valley vortex structure which is a characteristic of the subharmonic breakdown. In addition to the subharmonic and fundamental breakdown mechanisms, a combination resonance (or detuned secondary instability) studied extensively by Corke (1989) is also possible. In this mechanism, secondary disturbances consist of waves whose wavenumbers combine to yield the streamwise wavenumber of the primary two-dimensional wave. Corke concluded that a detuned mechanism leads to rapid filling of the spectrum and may be more relevant in natural transition.

Several direct numerical simulations (DNS) of the Navier–Stokes equations have

also been aimed at understanding the breakdown mechanisms of incompressible flat-plate boundary layers. For instance, Spalart & Yang (1987) studied the breakdown process associated with a finite-amplitude two-dimensional wave and low-amplitude three-dimensional random disturbances. Their results explain very well why fundamental breakdown was observed when the two-dimensional primary wave amplitude is large (Saric & Thomas 1984). Fasel, Rist & Konzelmann (1990) obtained good quantitative agreement for disturbance amplitudes with Kachanov & Levchenko's (1984) experiment. A recent review of the contribution of DNS to understanding the physics of transition is given by Kleiser & Zang (1991).

Compared to its low-speed counterpart, the transition mechanism in supersonic boundary layers remains poorly understood owing to the difficulties involved in instrumentation and the large amount of computational time required for direct numerical simulations. While a number of experiments have been performed on flat plates and cones in supersonic wind tunnels, they were all aimed at determining transition Reynolds numbers (e.g. Pate 1971; Chen, Malik & Beckwith 1989) as influenced by parameters such as wall temperature, nose bluntness, unit Reynolds numbers, etc. None of the experiments were focused on understanding the transition mechanism except for the experiments of Kendall (1967), who studied the evolution of first- and second-mode disturbances in the linear regime at Mach 4.5 using controlled disturbances, and Stetson (see Stetson & Kimmel 1992) at Mach 8. The results from other experiments at low supersonic Mach numbers (e.g. Laufer & Vrebalovich 1960; Kendall 1975; Demetriades 1989; Kosinov, Maslov & Shevelkov 1990) can best be described as 'inconclusive' owing to various experimental difficulties and/or the effects of noise radiated by the turbulent wind-tunnel wall boundary layers. Only in NASA Langley's Mach 3.5 'quiet' tunnel is this noise field eliminated by maintaining the tunnel walls laminar but, unfortunately, no fundamental transition physics experiment has been performed in this unique facility even in the linear regime. However, the transition Reynolds number on a flat-plate model was found to be about 12×10^6 in this wind tunnel as compared to only about 2.5×10^6 in conventional supersonic wind tunnels, which shows the dramatic effect free-stream disturbances can have on transition.

Temporal Navier–Stokes simulations are available from some authors (e.g. Erlebacher & Hussaini 1990; Pruett & Zang 1992) for supersonic and hypersonic flows. In these simulations, the time evolution of disturbances confined in a periodic box is studied under a quasi-parallel assumption. Qualitatively, temporal simulations offer a more economic way (since the spatial resolution required is minimal and the issues associated with boundary conditions in the streamwise direction are avoided) to help understand transition physics. However, in order to accurately describe the spatial evolution of disturbances and thereby provide a meaningful transition prediction, spatial simulations are needed. Owing to the increased demands on computational resources, only a limited number of compressible spatial simulations are available to date (e.g. Thumm, Wolz & Fasel 1989; Bestek, Thumm & Fasel 1992; Pruett & Chang 1993). The application of secondary instability theory to compressible flat-plate boundary layers has been carried out by El-Hady (1992), Masad & Nayfeh (1991) and Ng & Erlebacher (1992).

An alternative to spatial DNS is the newly emerging approach to transition studies based upon parabolized stability equations (PSE) (Herbert 1991; Chang *et al.* 1991; Bertolotti & Herbert 1991). In the PSE approach, the spatial evolution of disturbances is obtained by an efficient marching procedure which accounts for both nonlinear and non-parallel effects in the growing boundary layers. Linear and nonlinear PSE

calculations for incompressible and supersonic boundary layers yield results that are in remarkable agreement with those from spatial DNS (see Bertolotti, Herbert & Spalart 1992; Joslin, Streett & Chang 1993 and Pruett & Chang 1993) but at only a small fraction of the computational cost of the latter. This makes PSE a promising theoretical tool for transition research.

The main objective of this paper is to provide an in-depth study of the breakdown mechanisms in a supersonic flat-plate boundary layer using the PSE approach. Although the PSE method has been applied to second-mode disturbances in hypersonic flows (Chang & Malik 1993), here we will focus only on low-Mach-number supersonic flows and consider both subharmonic and fundamental secondary instabilities. For supersonic flows, the most amplified first-mode waves are oblique. Thus, these oblique modes will play an increasingly important role in the supersonic boundary-layer transition. One important feature of these oblique waves is that the interaction of a pair of oblique waves with opposite angles to the mean flow direction can produce a streamwise vortex. This streamwise vortex is damped linearly in the absence of concave surface curvature but, as we will show later, nonlinear interaction causes the streamwise vortex to grow at a rate which is much faster than that of the oblique wave itself and this strong growth initiates the oblique-mode breakdown process. Goldstein & Choi (1989) studied the nonlinear interaction of oblique waves in incompressible shear layers using asymptotic theory. They showed that three-dimensional effects cause nonlinearity to occur at much smaller amplitudes than it does in two-dimensional flows (see also Goldstein 1990). A brief account of the oblique breakdown for supersonic boundary-layer flows was earlier given by Chang & Malik (1992) (see also Bestek *et al.* 1992) but the present paper provides a much more comprehensive report on the subject. Here, PSE calculations are carried all the way into the transition regime where a sequence of instabilities results in breakdown of the laminar flow. These instabilities for a Mach 1.6 boundary layer are discussed and the relevance of the present calculations to the prediction of boundary-layer transition is brought out. We formulate the problem for compressible flow past a flat plate in §2, present and discuss the results in §3, while conclusions are drawn in §4.

2. Problem formulation

We consider supersonic boundary-layer flow over a flat plate with a sharp leading edge as shown in figure 1. For $M_\infty > 1$, a leading-edge shock is formed owing to the growing boundary layer. However, in the low supersonic regime, this shock is relatively weak and hence the Mach number behind the shock, M_e, is almost identical to the free-stream value, M_∞. In this paper, we focus on the instability waves and transition in the boundary-layer flow and effects of the weak leading-edge shock are neglected. As mentioned in §1, a comprehensive study of the transition mechanism should include the leading-edge receptivity process which occurs between $x^* = 0$ and $x^* = x_0^*$ (x_0^* is the streamwise coordinate of the critical region). In this paper, however, we do not consider the receptivity problem and assume that free-stream disturbances have already been internalized and the eigenstructure associated with boundary-layer instability waves exists at $x^* = x_0^*$ where they are about to enter the unstable regime. The boundary-layer instability problem to be studied in this paper therefore includes a computational domain which begins at x_0^* and stretches to x_{tr}^* where laminar–turbulent transition takes place. The domain height in the wall-normal direction is set at $y^* = y_{max}^*$, which increases downstream to accommodate the boundary-layer growth. Free-stream boundary conditions are enforced at $y^* = y_{max}^*$.

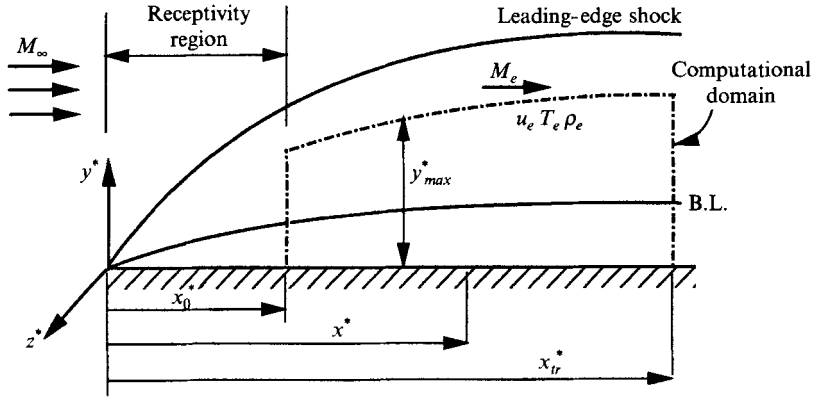

FIGURE 1. Schematic of supersonic flow over a sharp-leading-edge flat plate.

The evolution of disturbances in compressible boundary layers is governed by the compressible Navier–Stokes equations

$$\frac{\partial \rho^*}{\partial t^*} + \nabla\cdot(\rho^* V) = 0, \tag{2.1}$$

$$\rho^*\left[\frac{\partial V}{\partial t^*} + (V\cdot\nabla)\,V\right] = -\nabla p^* + \nabla[\lambda^*(\nabla\cdot V)] + \nabla\cdot[\mu^*(\nabla V + \nabla V^T)], \tag{2.2}$$

$$\rho^* c_p^*\left[\frac{\partial T^*}{\partial t^*} + (V\cdot\nabla)\,T^*\right] = \nabla\cdot(k^*\nabla T^*) + \frac{\partial p^*}{\partial t^*} + (V\cdot\nabla)p^* + \Phi^*, \tag{2.3}$$

where $V = (u^*, v^*, w^*)$ is the velocity vector, ρ^* the density, p^* the pressure, T^* the temperature, c_p^* the specific heat, k^* the thermal conductivity, μ^* the first coefficient of viscosity, and λ^* the second coefficient of viscosity. The viscous dissipation function is given as

$$\Phi^* = \lambda^*(\nabla\cdot V)^2 + \tfrac{1}{2}\mu^*[\nabla V + \nabla V^T]^2.$$

The equation of state is given by the perfect gas relation

$$p^* = \rho^* \Re T^*, \tag{2.4}$$

and the steady-state solution of the basic flow can be obtained by invoking the boundary-layer assumption.

2.1. *Compressible boundary-layer equations*

For boundary-layer flow over a flat plate, the governing equations can be derived by using the Levy–Lees transformation (see Hayes & Probstein 1959)

$$\mathrm{d}\xi = \rho_e^*\,\mu_e^*\,u_e^*\,\mathrm{d}x^*, \tag{2.5}$$

$$\mathrm{d}\eta = [\rho_e^*\,u_e^*/(2\xi)^{1/2}](\rho^*/\rho_e^*)\,\mathrm{d}y^*, \tag{2.6}$$

where all quantities with subscripts e represent the corresponding boundary-layer edge values. For a flat-plate boundary layer in the absence of a pressure gradient, the similarity flow is governed by the following equations in the transformed coordinates:

$$(\bar{c}f'')' + ff'' = 0, \tag{2.7}$$

$$(a_1 g' + a_2 f' f'')' + fg' = 0, \tag{2.8}$$

where $$f' = u^*/u_e^*, \quad \bar{c} = \rho^*\mu^*/\rho_e^*\mu_e^*, \quad g = H/H_e,$$

$$a_1 = \bar{c}/Pr, \quad a_2 = \frac{(\gamma-1)M_e^2}{1+\frac{1}{2}(\gamma-1)M_e^2}\left(1-\frac{1}{Pr}\right)\bar{c}.$$

In (2.7), both f and g are functions of η only. Here, the total enthalpy is denoted by H, the ratio of specific heats by γ, and the edge Mach number is defined as

$$M_e = \frac{u_e^*}{(\gamma \Re T_e^*)^{1/2}}.$$

The Prandtl number is defined as

$$Pr = \frac{\mu^* c_p^*}{k^*}.$$

In all the calculations herein (including basic flow and stability calculations), the viscosity μ^* is assumed to be given by the Sutherland law

$$\mu^* = 1.458 \times 10^{-5} \frac{T^{*1/2}}{1+110.4/T^*} \quad \text{N s m}^{-2}.$$

The thermal conductivity k^* can be computed by a similar formula. For the results presented in this paper, we assume a constant Prandtl number of 0.72. Stokes's hypothesis is used for the second coefficient of viscosity as

$$\lambda^* + 2/3\mu^* = 0.$$

The above similarity equations ((2.7)–(2.8)) are solved by a fourth-order-accurate compact-difference scheme (Malik, Chuang & Hussaini 1982) and Newton's method for the nonlinear iterations subject to no-slip wall boundary conditions. For the results presented in this paper, we use an adiabatic boundary condition for the wall temperature.

2.2. *Parabolized stability equations*

As shown in figure 1, the Cartesian coordinates are denoted by x^*, y^*, and z^* to represent the streamwise, wall-normal, and spanwise directions, respectively. All the lengths are scaled by a reference length l_0, velocity by u_e^*, density by ρ_e^*, pressure by $\rho_e^* u_e^{*2}$, time by l_0/u_e^*, and other variables by the corresponding boundary-layer edge values. The lengthscale l_0 to be used in all calculations presented in this paper is defined as

$$l_0 = (\nu_e^* x_0^*/u_e^*)^{1/2},$$

where x_0^* is the location where calculations are initiated and ν_e^* is the kinematic viscosity at the boundary-layer edge. All non-dimensional quantities after the above normalization will be denoted by the same symbol but without the asterisk.

The basic flow obtained by solving the boundary-layer equations (2.7) and (2.8) is perturbed by fluctuations in the flow, i.e. the total field can be decomposed into a mean value (boundary-layer solution) and a perturbation quantity:

$$\left.\begin{aligned} u &= \bar{u}+u', \quad v = \bar{v}+v', \quad w = 0+w', \\ p &= \bar{p}+p', \quad \rho = \bar{\rho}+\rho', \quad T = \bar{T}+T', \\ \mu &= \bar{\mu}+\mu', \quad \lambda = \bar{\lambda}+\lambda', \quad k = \bar{k}+k'. \end{aligned}\right\} \tag{2.9}$$

Substituting (2.9) into the Navier–Stokes and state equations given by (2.1)–(2.4) and subtracting the steady mean flow from it, we obtain the nonlinear disturbance equations as

$$\boldsymbol{\Gamma}\frac{\partial \boldsymbol{\phi}}{\partial t}+\boldsymbol{A}\frac{\partial \boldsymbol{\phi}}{\partial x}+\boldsymbol{B}\frac{\partial \boldsymbol{\phi}}{\partial y}+\boldsymbol{C}\frac{\partial \boldsymbol{\phi}}{\partial z}+\boldsymbol{D}\boldsymbol{\phi}$$
$$=\frac{1}{R_0}\left(\boldsymbol{V}_{xx}\frac{\partial^2 \boldsymbol{\phi}}{\partial x^2}+\boldsymbol{V}_{xy}\frac{\partial^2 \boldsymbol{\phi}}{\partial x\,\partial y}+\boldsymbol{V}_{yy}\frac{\partial^2 \boldsymbol{\phi}}{\partial y^2}+\boldsymbol{V}_{xz}\frac{\partial^2 \boldsymbol{\phi}}{\partial x\,\partial z}+\boldsymbol{V}_{yz}\frac{\partial^2 \boldsymbol{\phi}}{\partial y\,\partial z}+\boldsymbol{V}_{zz}\frac{\partial^2 \boldsymbol{\phi}}{\partial z^2}\right), \quad (2.10)$$

where $\boldsymbol{\phi}$ contains the disturbance vector and is defined as

$$\boldsymbol{\phi}=(\rho', u', v', w', T')^T.$$

The scaling Reynolds number R_0 is defined based upon the boundary-layer lengthscale at x_0^* as

$$R_0=u_e^* l_0/\nu_e^*,$$

while for the results to be presented in §3, we use a streamwise Reynolds number defined as

$$R=u_e^* l_x/\nu_e^*,$$

where the local lengthscale l_x is based upon the local x^* coordinate as

$$l_x=(\nu_e^* x^*/u_e^*)^{1/2}.$$

Matrices $\boldsymbol{\Gamma}$, $\boldsymbol{A}$, $\boldsymbol{B}$, $\boldsymbol{C}$, $\boldsymbol{D}$, $\boldsymbol{V}_{xx}$, $\boldsymbol{V}_{xy}$, $\boldsymbol{V}_{yy}$, $\boldsymbol{V}_{xz}$, $\boldsymbol{V}_{yz}$, and $\boldsymbol{V}_{zz}$ are Jacobians of the corresponding total flux vectors and are composed of a linear part with only mean flow quantities (denoted by superscripts l below) and a nonlinear part which contains perturbation quantities (denoted by superscripts n below). We note here that matrices $\boldsymbol{\Gamma}$, $\boldsymbol{A}$, $\boldsymbol{B}$, $\boldsymbol{C}$, $\boldsymbol{D}$ have contributions from both inviscid and viscous terms, and thus contain terms of order one and of order $1/R_0$, while the right-hand side of (2.10) contains terms which are solely due to viscous effects.

We assume that the given disturbance is periodic in time and in the spanwise direction; thus, the disturbance function $\boldsymbol{\phi}$ can be expressed by the following Fourier series:

$$\boldsymbol{\phi}=\sum_{m=-\infty}^{\infty}\sum_{n=-\infty}^{\infty}\chi_{mn}(x,y)\,\mathrm{e}^{\mathrm{i}(n\beta z-m\omega t)}. \quad (2.11)$$

Here, the frequency ω and wavenumber β are chosen such that the longest period and wavelength are $2\pi/\omega$ and $2\pi/\beta$ in the temporal and spanwise domains, respectively. For most stability problems of interest, it is sufficient to truncate (2.11) to only a finite number of modes,

$$\boldsymbol{\phi}=\sum_{m=-M}^{M}\sum_{n=-N}^{N}\chi_{mn}(x,y)\,\mathrm{e}^{\mathrm{i}(n\beta z-m\omega t)}, \quad (2.12)$$

where M and N represent one-half the number of modes kept in the truncated Fourier series.

In linear as well as nonlinear stability problems, we are interested in the evolution of χ_{mn} along the streamwise direction. Within the framework of DNS, this evolution is obtained by numerically solving the governing equations for χ_{mn} (most simulations use discretization in time and solve for Fourier coefficients in the spanwise direction only). Since the Fourier expansion does not alter the characteristics of the Navier–Stokes equations, numerical solutions of the elliptic governing equations for

χ_{mn} are computationally expensive. Furthermore, because of the wave nature of the disturbances, χ_{mn} in general evolves as an oscillatory wave which grows (or decays) in the streamwise direction. To resolve these oscillatory motions for different Fourier modes whose amplitudes may vary by orders of magnitude in the computational domain, a highly accurate scheme and properly refined grid must be used. Consequently, an enormous amount of computational time is unavoidable. In the PSE approach, instead of solving for χ_{mn} directly, we adopt the idea of the multiple-scales method and further decompose χ_{mn} into a fast varying wave-like part and a slowly varying shape function and write χ_{mn} as

$$\chi_{mn}(x,y) = \Psi_{mn}(x,y)\,\mathscr{A}_{mn}(x), \tag{2.13}$$

$$\mathscr{A}_{mn}(x) = \exp\left[\mathrm{i}\int_{x_0}^{x} \alpha_{mn}(\bar{x})\,\mathrm{d}\bar{x}\right], \tag{2.14}$$

where Ψ_{mn} is the shape function for the Fourier mode $(m\omega, n\beta)$ and α_{mn} is the associated streamwise (complex) wavenumber. The notion here is to include the oscillatory motion in the wave part and solve only the evolution of the shape functions. Since the oscillatory motion is 'absorbed' by a properly chosen α_{mn} (see discussion below), the shape functions would evolve slowly along the streamwise direction and thus alleviate the high-resolution requirement in the direct approach and significantly reduce the computational cost. The required computational effort is further reduced by invoking a parabolizing approximation of the governing equations for the shape functions, which will be discussed below.

Upon substitution of (2.13), (2.14) together with (2.12) into the partial differential equations (2.10), we have the governing equations for shape functions of the (m,n) Fourier mode as

$$\hat{\boldsymbol{D}}_{mn}\Psi_{mn} + \hat{\boldsymbol{A}}_{mn}\frac{\partial \Psi_{mn}}{\partial x} + \hat{\boldsymbol{B}}_{mn}\frac{\partial \Psi_{mn}}{\partial y} - \frac{1}{R_0}\left(\boldsymbol{V}^l_{xx}\frac{\partial^2 \Psi_{mn}}{\partial x^2} + \boldsymbol{V}^l_{xy}\frac{\partial^2 \Psi_{mn}}{\partial x\,\partial y} + \boldsymbol{V}^l_{yy}\frac{\partial^2 \Psi_{mn}}{\partial y^2}\right) = \frac{\boldsymbol{F}_{mn}}{\mathscr{A}_{mn}}, \tag{2.15}$$

where matrices $\hat{\boldsymbol{D}}_{mn}$, $\hat{\boldsymbol{A}}_{mn}$, and $\hat{\boldsymbol{B}}_{mn}$ are given by

$$\hat{\boldsymbol{D}}_{mn} = -\mathrm{i}m\omega\boldsymbol{\Gamma}^l + \boldsymbol{D}^l + \mathrm{i}\alpha_{mn}\boldsymbol{A}^l + \mathrm{i}n\beta\boldsymbol{C}^l - (\mathrm{i}\,\mathrm{d}\alpha_{mn}/\mathrm{d}x - \alpha_{mn}^2)\,\boldsymbol{V}^l_{xx}/R_0 + n\alpha_{mn}\beta\boldsymbol{V}^l_{xz}/R_0 + n^2\beta^2\boldsymbol{V}^l_{zz}/R_0,$$

$$\hat{\boldsymbol{A}}_{mn} = \boldsymbol{A}^l - 2\mathrm{i}\alpha_{mn}\boldsymbol{V}^l_{xx}/R_0 - \mathrm{i}n\beta\boldsymbol{V}^l_{xz}/R_0,$$

$$\hat{\boldsymbol{B}}_{mn} = \boldsymbol{B}^l - \mathrm{i}\alpha_{mn}\boldsymbol{V}^l_{xy}/R_0 - \mathrm{i}n\beta\boldsymbol{V}^l_{yz}/R_0.$$

The left-hand side of (2.15) contains only linear coefficient matrices and all nonlinear terms are included in the forcing function $\boldsymbol{F}_{mn}$ which is the Fourier component of the total forcing, $\boldsymbol{F}^n$, defined as

$$\boldsymbol{F}^n = -\boldsymbol{\Gamma}^n\frac{\partial \boldsymbol{\phi}}{\partial t} - \boldsymbol{A}^n\frac{\partial \boldsymbol{\phi}}{\partial x} - \boldsymbol{B}^n\frac{\partial \boldsymbol{\phi}}{\partial y} - \boldsymbol{C}^n\frac{\partial \boldsymbol{\phi}}{\partial z} - \boldsymbol{D}^n\boldsymbol{\phi} + \frac{1}{R_0}\left(\boldsymbol{V}^n_{xx}\frac{\partial^2 \boldsymbol{\phi}}{\partial x^2} + \boldsymbol{V}^n_{xy}\frac{\partial^2 \boldsymbol{\phi}}{\partial x\,\partial y} + \boldsymbol{V}^n_{yy}\frac{\partial^2 \boldsymbol{\phi}}{\partial y^2} + \boldsymbol{V}^n_{xz}\frac{\partial^2 \boldsymbol{\phi}}{\partial x\,\partial z} + \boldsymbol{V}^n_{yz}\frac{\partial^2 \boldsymbol{\phi}}{\partial y\,\partial z} + \boldsymbol{V}^n_{zz}\frac{\partial^2 \boldsymbol{\phi}}{\partial z^2}\right),$$

where all matrices with superscripts n denote corresponding coefficients containing

dependent variables $\boldsymbol{\phi}$ (nonlinear terms). The quantity $\boldsymbol{F}^n$ is defined in physical space and can be evaluated by the Fourier series expansion

$$\boldsymbol{F}^n(x,y,z,t) = \sum_{m=-M}^{M} \sum_{n=-N}^{N} \boldsymbol{F}_{mn}(x,y)\, \mathrm{e}^{\mathrm{i}(n\beta z - m\omega t)}. \tag{2.16}$$

Computationally, the Fourier decomposition of (2.16) can be done by using the fast Fourier transform (FFT) of $\boldsymbol{F}^n$, which is evaluated numerically in the physical space. The corresponding linear PSE can be obtained by setting $\boldsymbol{F}_{mn}$ to zero in (2.15).

In the quasi-parallel compressible linear stability theory (Mack 1969) where 'normal-mode' analysis is employed, the shape function Ψ (for any given Fourier mode (m,n)) is assumed to be a function of y only ($\mathrm{d}\Psi/\mathrm{d}x = 0$); therefore, (2.15) reduces to the following system of ODE's:

$$\mathrm{L}_0\, \Psi = 0, \tag{2.17}$$

where the operator L_0 is given by

$$\mathrm{L}_0 = \hat{\boldsymbol{D}} + \hat{\boldsymbol{B}} \frac{\mathrm{d}}{\mathrm{d}y} - \frac{\boldsymbol{V}^l_{yy}}{R_0} \frac{\mathrm{d}^2}{\mathrm{d}y^2}$$

and the elements of matrices $\hat{\boldsymbol{D}}$, $\hat{\boldsymbol{B}}$ and $\boldsymbol{V}^l_{yy}$ are evaluated by assuming parallel mean flows ($\bar{v} = 0$, $\mathrm{d}\bar{u}/\mathrm{d}x = 0$, etc. and $\mathrm{d}\alpha/\mathrm{d}x = 0$). In the above equation, subscripts mn are dropped for simplicity. The above ODE's in conjunction with homogeneous boundary conditions then constitute an eigenvalue problem of the linear stability theory (see Malik 1990 for elements of matrices $\hat{\boldsymbol{D}}$, $\hat{\boldsymbol{B}}$ and $\boldsymbol{V}^l_{yy}$).

Unlike the normal-mode analysis described above where the complex wavenumber α_{mn} is determined from the eigenvalue analysis, the decomposition (2.13) is not uniquely defined as one can arbitrarily alter the distribution of the wave part and the shape function part. In the PSE approach, we choose a complex wavenumber α_{mn} and construct the decomposition (2.13) such that the change of shape functions Ψ_{mn} along the streamwise direction x is of order $1/R_0$ and the second derivative of Ψ_{mn} ($\partial^2\Psi_{mn}/\partial x^2$) is negligible. With this assumption and after neglecting all terms of $O(1/R_0^2)$, (2.15) reduces to

$$\hat{\boldsymbol{D}}_{mn}\, \Psi_{mn} + \hat{\boldsymbol{A}}_{mn} \frac{\partial \Psi_{mn}}{\partial x} + \hat{\boldsymbol{B}}_{mn} \frac{\partial \Psi_{mn}}{\partial y} = \frac{\boldsymbol{V}^l_{yy}}{R_0} \frac{\partial^2 \Psi_{mn}}{\partial y^2} + \frac{\boldsymbol{F}_{mn}}{\mathscr{A}_{mn}}. \tag{2.18}$$

Equation (2.18) describes the evolution of the shape function Ψ_{mn} and is 'nearly' parabolic in the sense that second derivatives in x (associated with streamwise viscous diffusion) are absent and the elliptic effect associated with the wave part is absorbed in matrices $\hat{\boldsymbol{D}}_{mn}$, $\hat{\boldsymbol{A}}_{mn}$ and $\hat{\boldsymbol{B}}_{mn}$. We note that in addition to the streamwise viscous diffusion, the upstream acoustic wave which is still present in the above formulation is also responsible for the elliptic effect. This upstream wave propagation is associated with the left-running characteristic in the (x,t)-plane for the inviscid Euler equations (i.e. the left-hand side of (2.10)). Within the framework of inviscid gas dynamics, it can be shown that when the flow is subsonic, there exists an upstream acoustic wave which makes the Euler equations elliptic. Owing to its inviscid origin, the upstream acoustic wave (and the elliptic effect) is always present regardless of the approximation on the streamwise viscous diffusion. Therefore, an additional approximation is needed for a stable marching solution.

For compressible flows, the upstream acoustic wave arises as a characteristic of the Euler equations and all inviscid terms contribute to it. However, one can make approximation to the pressure gradient term in the streamwise momentum equation

and alter the left-running characteristic as is done in the parabolized Navier–Stokes (PNS) equations (see Vigneron, Rakich & Tannehill 1978). For the partially parabolized equations, (2.18), we consider the streamwise momentum equation which contains the pressure gradient term $\partial p'/\partial x$ written here as

$$\frac{\partial p'_{mn}}{\partial x} = \left(\mathrm{i}\alpha_{mn}\hat{p}_{mn} + \Omega\frac{\partial \hat{p}_{mn}}{\partial x}\right)\exp\left[\mathrm{i}\left(\int_{x_0}^{x}\alpha_{mn}(\bar{x})\,\mathrm{d}\bar{x} + n\beta z - m\omega t\right)\right], \tag{2.19}$$

where Ω is a multiplier yet to be defined. Note that the contribution of the wave part ($\mathrm{i}\alpha\hat{p}_{mn}$) is absorbed in the source term $\hat{\boldsymbol{D}}_{mn}\boldsymbol{\Psi}_{mn}$ in (2.18). If $\Omega = 1$, the pressure-gradient term is completely retained and $\partial\hat{p}_{mn}/\partial x$ allows upstream acoustic propagation. For incompressible flow, it can be shown (Li & Malik 1992) by using Fourier stability analysis that the condition for numerical stability requires that no more than 2π steps per TS wavelength should be taken for a marching solution (i.e. $\alpha\Delta x > 1$ where Δx is the marching step size). Fourier analysis of the compressible system (2.18) (as well as numerical experiments) also reveals that marching solutions are stable only when $\alpha\Delta x$ is greater than a threshold value. This threshold value depends upon various factors such as Mach number, grid aspect ratio and disturbance frequency, etc. The step size limitation is not severe as computations show that a PSE solution with only 3 steps per TS wavelength agrees very well with a higher-order DNS solution using 60 grid points per wavelength.

For supersonic flows, the upstream influence through the $\partial\hat{p}_{mn}/\partial x$ term is possible only in the subsonic layer near the wall. To obtain a stable marching solution without step size limitation, we choose the Ω value in (2.19) according to an approximation suggested by Vigneron *et al.* (1978) for mean flow computations using the PNS equations. This approximation suppresses part of the pressure-gradient term in the streamwise momentum equation by selecting Ω according to

$$\begin{aligned}\Omega &= \frac{\gamma M_x^2}{1+(\gamma-1)M_x^2}, \quad && M_x < 1,\\ &= 1, && M_x \geqslant 1,\end{aligned} \tag{2.20}$$

where M_x is the local (y-dependent) Mach number in the boundary layer. In the supersonic portion of the boundary layer, no additional approximation is made since $\Omega = 1$. The net effect on the subsonic portion is that characteristic eigenvalues of the governing equations are all positive (right-running) and the upstream influence is suppressed. For a stable marching solution of the PSE without step size limitation, we evaluate Ω from (2.20) and use it in (2.19).

In the incompressible limit, the use of Ω in (2.19) is equivalent to setting $\partial\hat{p}_{mn}/\partial x$ to zero. While this is formally true only in special cases (e.g. the Görtler vortex problem), the approximation yields solutions which compare very well with accurate results from the full Navier–Stokes equations (Joslin *et al.* 1993). This is because most of the ellipticity is captured in the $\mathrm{i}\alpha\hat{p}_{mn}$ term. The resulting parabolized governing equations for the shape functions thus can be solved by an efficient marching procedure along the streamwise direction. For compressible flows, linear and nonlinear PSE results with the above approximation have been compared with compressible spatial DNS (Pruett & Chang 1993) with remarkably good agreement; however, while DNS required about 30 hours of Cray-YMP time, a comparable PSE solution was obtained in less than 2 minutes.

The choice of α_{mn} plays a crucial role in the accuracy of the parabolizing approximation. We now describe the approach we take to determine α_{mn}. The

evolution of shape functions is monitored during the process of marching and α_{mn} is updated by local iterations at a given x according to the change in a selected dependent variable, say Ψ_1. At a given location x_1, we assume that the streamwise wavenumber is given by α_1. An 'effective' wavenumber is then evaluated based on

$$\alpha = \alpha_1 - \mathrm{i}\frac{1}{\Psi_1}\frac{\mathrm{d}\Psi_1}{\mathrm{d}x}. \tag{2.21}$$

The real part of this effective wavenumber represents the phase change of the disturbance while the imaginary part gives the growth rate, both corresponding to the variable Ψ_1 chosen. A disturbance (Ψ_1) is unstable if the imaginary part is less than zero. The updating procedure for α is repeated by using (2.21) until the change in α is smaller than a prescribed tolerance (typically 10^{-12}).

Since the shape function vector Ψ_{mn} is a function of y and contains five dependent variables ($\hat{\rho}, \hat{u}$, etc.), the updating procedure above is equivalent to choosing a normalization of the disturbance vector such that $\mathrm{d}\Psi_1/\mathrm{d}x$ is zero at a particular y-location. Accordingly, the value of α computed by (2.21) depends on the y-coordinate and the selected dependent variable Ψ_1. In this study, therefore, we use the following expression to determine α:

$$\alpha = \alpha_1 - \mathrm{i}\frac{1}{E}\int_0^\infty \bar{\rho}\left(\hat{u}^\dagger\frac{\partial\hat{u}}{\partial x} + \hat{v}^\dagger\frac{\partial\hat{v}}{\partial x} + \hat{w}^\dagger\frac{\partial\hat{w}}{\partial x}\right)\mathrm{d}y, \tag{2.22}$$

where superscripts $\dagger$ denote complex conjugates and E is given as

$$E = \int_0^\infty \bar{\rho}(|\hat{u}|^2 + |\hat{v}|^2 + |\hat{w}|^2)\,\mathrm{d}y,$$

which is independent of the y-coordinate.

As shown in figure 1, the streamwise computational domain extends from x_0^* to any arbitrary x^*. It was pointed out that there is an implicit assumption that the disturbance already exists in the boundary layer in the form of an eigensolution at $x^* = x_0^*$. Leading-edge receptivity due to free-stream acoustic waves and the excitation of instability waves via the interaction of surface non-uniformity and unsteady free-stream disturbance in supersonic boundary layers have been studied by Fedorov & Khokhlov (1991, 1992) and Choudhari & Streett (1993). In this paper, the effect of initial amplitude at x_0^* is studied by choosing different amplitude combinations of the fundamental Fourier modes selected in the nonlinear calculations. The solution of (2.18) also requires proper boundary conditions in the wall-normal direction. We apply the homogeneous Dirichlet conditions

$$\hat{u} = \hat{v} = \hat{w} = \hat{T} = 0, \quad y = 0 \tag{2.23}$$

at the wall and in the free stream

$$\hat{u} = \hat{v} = \hat{w} = \hat{T} = 0, \quad y \to \infty; \tag{2.24}$$

although these can be easily replaced by other conditions such as the Rankine–Hugoniot conditions at the shock (Chang, Malik & Hussaini 1990) for supersonic flows.

For nonlinear calculations, (2.18) is solved for all Fourier modes subject to boundary conditions (2.23) and (2.24), except for the mean flow distortion mode, (0, 0). For this mode, we replace the boundary condition at the far field, (2.24), by

$$\hat{u}_{00} = \frac{\partial\hat{v}_{00}}{\partial y} = \hat{w}_{00} = \hat{T}_{00} = 0, \quad y \to \infty \tag{2.25}$$

to account for the change of displacement thickness due to the distortion of the mean flow profile ($\bar{u}+\hat{u}_{00}$) arising from nonlinear interactions. This Neumann condition for the normal velocity allows the mean flow given by the boundary-layer solution to adjust itself in order to assure mass balance.

Numerical solution of the parabolized stability equations (2.18) requires discretization in both x- and y-directions. Since the boundary layer grows in the streamwise direction, we expect that the solution for the shape functions will also grow. To ensure sufficient resolution as the disturbances evolve downstream, discretization in the wall-normal direction must be able to account for the growth of the boundary layer. Instead of solving (2.18) in Cartesian coordinates, we transform these equations to a generalized coordinate system and discretize the streamwise derivatives by a backward Euler differencing and wall-normal derivatives by a fourth-order-accurate finite-difference scheme.

3. Results and discussion

All the calculations presented in this paper have been made for a flat-plate boundary layer at adiabatic wall conditions. The boundary-layer edge Mach number is taken to be 1.6 and the edge temperature is 300 K. We first briefly discuss the linear stability of this boundary layer and the nonlinear development and secondary instabilities will follow.

3.1. *Linear stability*

It is useful to first give some results from linear theory to determine the range of unstable disturbance frequencies. Figure 2 gives the neutral curves for the wave angles of 0°, 40°, 50° and 60° in the frequency–Reynolds number plane where the non-dimensional frequency F is defined as

$$F = 2\pi\nu_e^* f^{(Hz)}/(u_e^*)^2$$

and the Reynolds number R is the local value as defined in §2.2. Some of the frequencies for which nonlinear PSE calculations will be performed have been marked on the plot. These neutral curves have been computed using quasi-parallel theory (equation (2.17)). The boundaries of the unstable region in figure 2 will shift somewhat owing to non-parallel effect. In figure 3, we plot linear PSE results for the integrated growth $N_{\rho u}$ defined as

$$N_{\rho u} = \int_{x_0}^{x} \sigma_{\rho u}\, \mathrm{d}\bar{x}, \tag{3.1}$$

where $\sigma_{\rho u}$ is the total non-parallel growth rate measured at the location of the peak mass flow fluctuation. As is evident from figure 3, the neutral locations have shifted slightly as a result of the boundary-layer growth and the total growth of oblique disturbances is considerably higher than that of two-dimensional disturbances. For this case, the non-parallel effect (which is accounted for in the PSE calculation) is destabilizing for oblique disturbances and is slightly stabilizing for the two-dimensional disturbance.

3.2. *Secondary instability*

In this section, we first consider the nonlinear interaction of two-dimensional and three-dimensional waves. We set up the problem in the framework of PSE by including in the initial conditions a two-dimensional wave (mode (2, 0)) with a frequency of $F = 0.4 \times 10^{-4}$ and two pairs of three-dimensional disturbances with equal spanwise wavenumbers of $\beta/R = \pm 0.96 \times 10^{-4}$ and frequencies of 0.4×10^{-4} (mode (2, 1) and

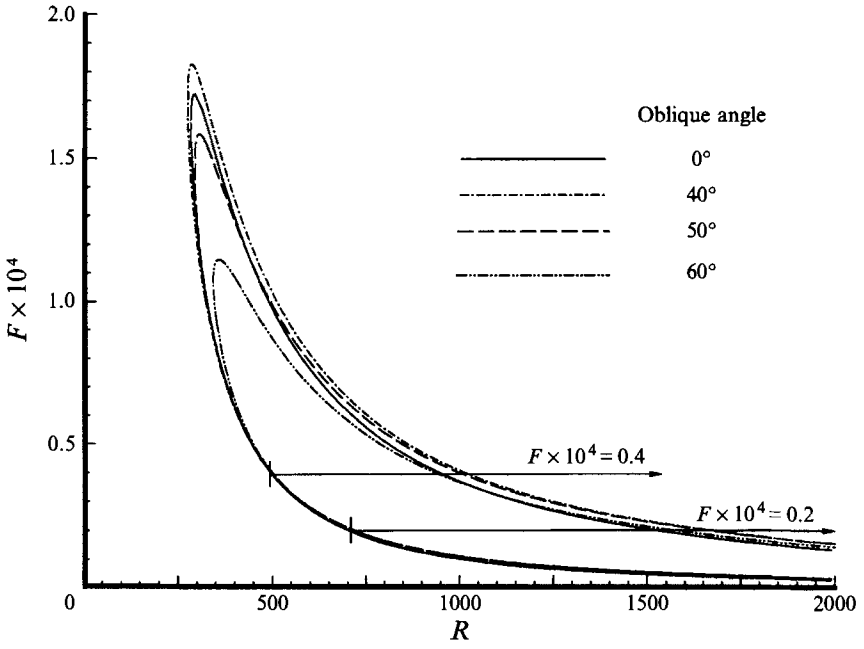

FIGURE 2. Neutral curves for Mach 1.6 flat-plate boundary layer.

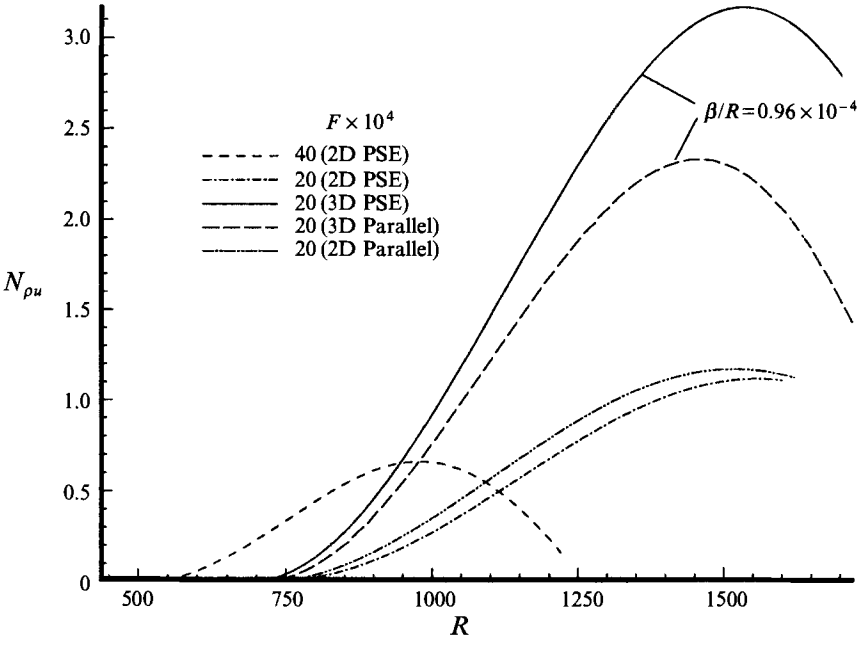

FIGURE 3. Non-parallel N factor from linear PSE solutions for various two-dimensional and oblique disturbances.

$(2, -1))$ and 0.2×10^{-4} (mode $(1, 1)$ and $(1, -1)$), corresponding to fundamental and subharmonic secondary disturbances, respectively. The initial conditions of all three modes are generated by performing local linear (non-parallel) eigenvalue calculations at the inflow plane which in this case is located at $R = 520$ where the two-dimensional wave just enters the unstable regime. The selected spanwise wavenumber corresponds

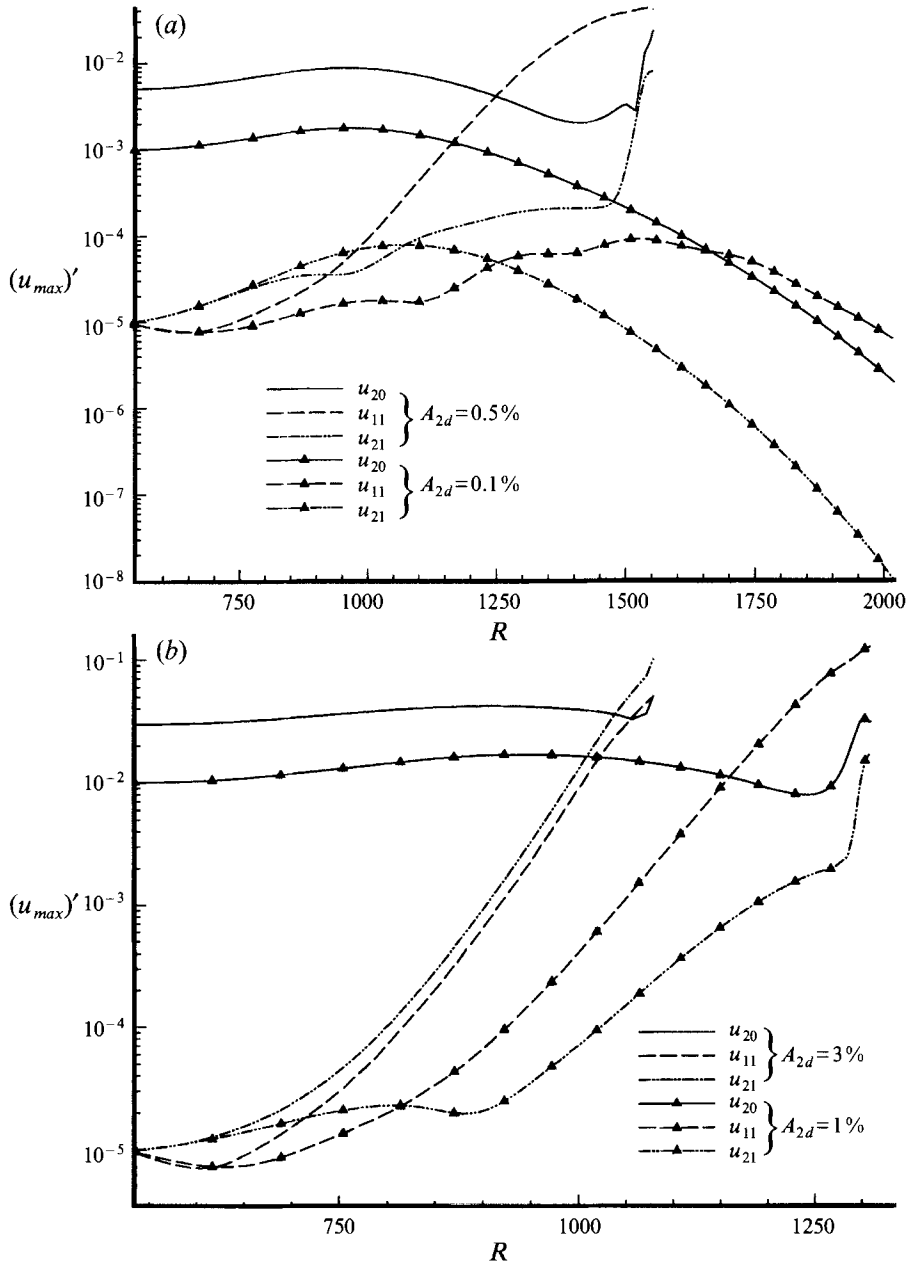

FIGURE 4. Evolution of maximum r.m.s. u-velocity perturbations for various two-dimensional wave amplitudes: (*a*) $A_{2d} = 0.5\%, 0.1\%$; (*b*) $A_{2d} = 3\%, 1\%$.

to wave angles of 47° and 65° for the fundamental and subharmonic modes, respectively, at the inflow plane. Self-interaction of the (1, 1) mode would excite the (2, 2) mode which can also be considered as a fundamental secondary disturbance.

For all nonlinear results presented herein, we refer to the amplitude of any Fourier mode as the r.m.s. value defined as

$$A_{mn} = \left(\frac{1}{\tau}\int_0^{\tau} \phi_{mn}^2 \, \mathrm{d}t\right)^{1/2}, \tag{3.2}$$

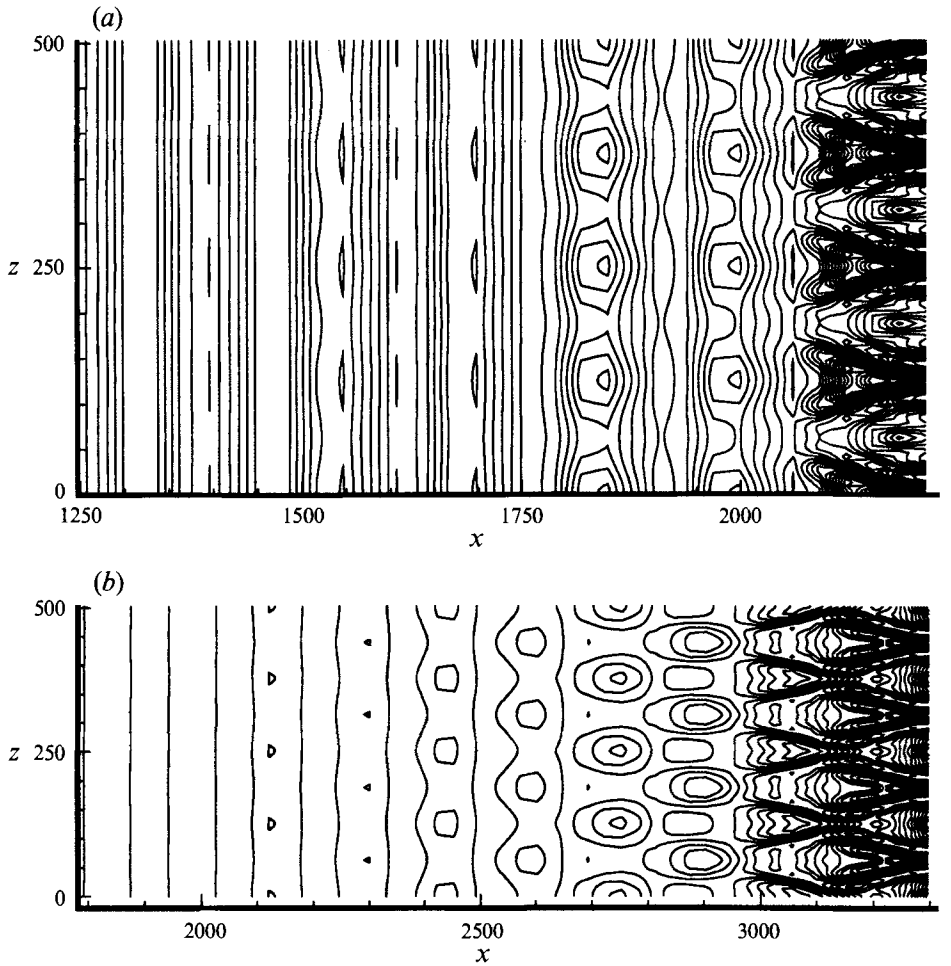

FIGURE 5. Instantaneous u-velocity contours in the (x, z)-plane at $y^*/l_x = 2.3$ for two different two-dimensional wave amplitudes: (*a*) $A_{2d} = 3\%$, (*b*) $A_{2d} = 1\%$.

where $\tau = 2\pi/\omega$ is the time period associated with the computational domain. The quantity ϕ_{mn} is the amplitude of the Fourier component of the total perturbation (as defined in (2.12)),

$$\phi_{mn} = |(\chi_{mn})_{max}\, e^{i(n\beta z - m\omega t)}|, \tag{3.3}$$

measured at the corresponding peak location in the wall-normal direction. From linear stability theory (as well as linear PSE), maximum fluctuation occurs in the streamwise velocity perturbation among all flow variables at Mach 1.6. Therefore, we use the u-velocity component in (3.2) to represent the evolution of the disturbance field in the nonlinear results and initial conditions are input based upon the r.m.s. amplitude of the u velocity.

Both secondary disturbances are assigned an initial amplitude (A_{3d}) of 0.001% and the amplitude of the two-dimensional wave (A_{2d}) is varied from 0.1% to 3%, in order to study the effect of the amplitude of the two-dimensional wave on secondary instability. It is known that in incompressible flow, secondary instability is present even for very small initial A_{2d}. Seven temporal modes and five spanwise modes ($M = 7$, $N = 5$) are used in the present calculations. Figures 4(*a*) and 4(*b*) show the resulting maximum r.m.s. amplitudes of the u-velocity perturbation for the three externally

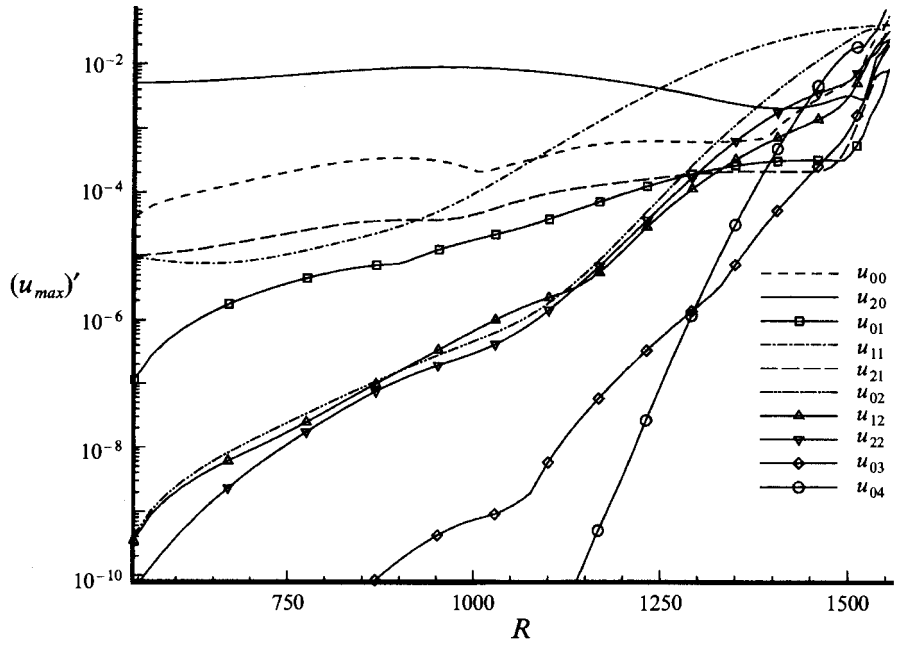

FIGURE 6. Evolution of maximum r.m.s. u-velocity perturbations for various Fourier modes for $A_{2d} = 0.5\%$.

excited modes, (2, 0), (1, 1) and (2, 1). For the $A_{2d} = 0.1\%$ case, there is mild growth of the subharmonic disturbance but it eventually dies out. Strong growth of secondary disturbances is evident only for the cases with A_{2d} equal to or greater than 0.5%. For the 3% case, both subharmonic and fundamental secondary modes grow rapidly and the (2, 1) mode has slightly higher amplitude than the (1, 1) mode, indicating a mixed subharmonic–fundamental secondary instability. For the remaining two cases ($A_{2d} = 0.5\%$ and 1%), the subharmonic mode (1, 1) exhibits much stronger growth than the (2, 1) mode and the subharmonic-type instability prevails.

To further demonstrate that the dominant breakdown mechanism switches from subharmonic to fundamental type as the TS wave amplitude is increased, we plot the streamwise velocity contours in the (x, z)-plane at a normal distance of $y^*/l_x = 2.3$ near the critical layer in figures 5(a) and 5(b). Both x- and z-coordinates are normalized with l_0, the boundary-layer lengthscale at $R = 520$; thus $x = R^2/R_0$. For the 3% case, an aligned lambda vortex pattern is present near the end of the simulation although the amplitude evolution (figure 4b) shows a mixed subharmonic–fundamental-type instability, while in the 1% case a subharmonic-type staggered contour pattern is clearly evident. These results are consistent with the incompressible experiment of Saric & Thomas (1984) where it was found that by increasing the amplitude of the two-dimensional TS wave, the dominating mechanism is shifting from subharmonic to fundamental breakdown. Similarly, Corke & Mangano's (1989) experiment was done with a low-amplitude TS wave; therefore, no fundamental mechanism was observed.

To explore in more detail the evolution of various disturbance modes, we plot the maximum u-velocity r.m.s. amplitude of various Fourier modes for the 0.5% case in figure 6. Unlike the subharmonic instability where the spectrum shows a staggered pattern, all harmonic waves are excited owing to the presence of fundamental mode (2, 1). Among the harmonic waves shown in the figure, mode (0, 1) gains energy from the interaction of (2, 0) and (2, 1). Similarly, mode (1, 2) (from (2, 1) − (1, −1)), (2, 2)

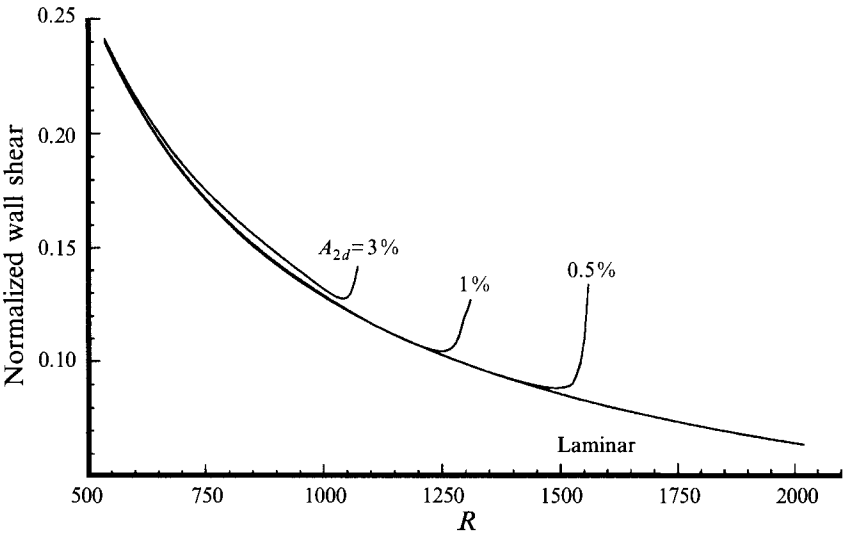

FIGURE 7. Average wall shear versus Reynolds numbers for various two-dimensional wave amplitudes compared with the unperturbed laminar solution.

(from $(1,1)+(1,1)$), and $(0,2)$ (from $(1,1)+(-1,1)$ and $(2,1)+(-2,1)$) are excited early in the simulation. The subharmonic mode overtakes the primary wave at about $R = 1200$ and tends to saturate towards the end of the calculation while the streamwise vortex modes $(0,2)$ and $(0,4)$ continue to grow very rapidly. Near the end, the damped primary wave (which has passed the upper-branch neutral point) and the other harmonics (e.g. $(0,1)$ and $(2,1)$) undergo fast growth because the subharmonic and streamwise vortex modes have reached very large amplitudes (on the order of a few percent). This fast growth triggers a spectrum broadening and the flow is heading towards transition.

To determine the location of transition onset, we plot the average wall shear versus Reynolds number for the above three cases (namely $A_{2d} = 0.5\%$, 1% and 3%) in figure 7. One clearly sees the rapid rise of shear stress indicating the onset of transition. For the 0.5% case, transition occurs at a Reynolds number R of about 1500 which corresponds to the plate-length Reynolds number of 2.25×10^6, a typical value found in conventional supersonic wind tunnel experiments. Near the transition onset $R = 1500$, the maximum streamwise velocity perturbation has reached an amplitude of about 3.7% for the subharmonic component. For the case of $A_{2d} = 1\%$, this amplitude is about 5%. For $A_{2d} = 3\%$, the amplitude of the fundamental mode is also 5% (figure 4*b*). Thus in these three cases, the amplitude of the most energetic mode is in the range of 3.7–5% at the onset of transition.

One major assumption in the Floquet-based secondary instability theory is that the primary disturbance remains unaffected during the rapid secondary disturbance growth. In the PSE framework, such an assumption is not needed and the backreaction can be captured in the analysis. In figure 8, we compare the above $A_{2d} = 0.5\%$ results with the corresponding linear PSE solutions for modes $(2,0)$, $(1,1)$ and $(2,1)$. It is clearly seen that the primary TS wave follows the linear growth for quite a long distance while the subharmonic wave departs from its linear solution right after the onset of secondary instability at $R = 700$. During the rapid growth of the subharmonic mode ($700 < R < 1400$), the primary two-dimensional wave follows linear growth, showing essentially no backreaction. The fundamental mode $(2,1)$ initially grows

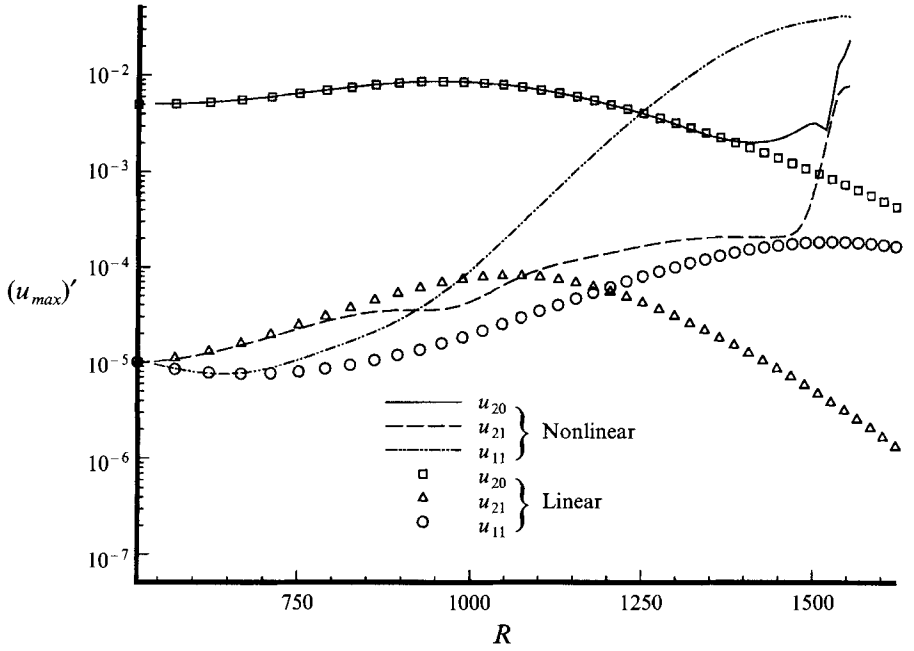

FIGURE 8. Comparison of linear and nonlinear u-velocity amplitude evolution for the $A_{2d} = 0.5\%$ case.

slower than the linear rate but beyond the upper (linear) neutral point it continues to grow modestly. At a Reynolds number of 1400, the subharmonic mode has reached an amplitude of about 2%. Beyond this Reynolds number, the two-dimensional primary wave starts to deviate from its linear solution and, as shown in figure 6, other harmonics including the (2, 1) mode grow very rapidly. In this regime, the backreaction has forced the primary wave to be re-energized and the highly nonlinear nature of the disturbance field makes the secondary instability theory invalid. Similar backreaction and re-amplification of the primary disturbance has also been observed in incompressible Navier–Stokes simulations (e.g. Spalart & Yang 1987; Zang & Hussaini 1990).

The amplitude evolution in figure 6 only shows maximum velocity perturbations. To better visualize the evolution of velocity shape functions, we plot the profiles of the u-velocity perturbation for (2, 0), (1, 1) and mean-flow distortion (MFD) modes at various locations in figures 9(*a*), 9(*b*) and 9(*c*), respectively. The y-coordinate shown in these figures has been normalized with respect to the lengthscale l_0 at $R = 520$. The peak amplitude of the primary mode occurs near the wall and shifts outwards as the boundary layer grows. Although the peak of the primary mode grows (and decays) linearly for $R < 1400$ (as in figure 8), the nonlinear effect has distorted the profile, resulting in a second hump (for $R = 1100$, 1251, 1349) below the maximum location, invalidating the shape assumption of the Floquet-based secondary instability theory. The subharmonic profiles shown in figure 9(*b*) have similar shapes for all six locations. The peak of this mode occurs at $y^*/l_x = 2.5$ (l_x is the local boundary-layer lengthscale defined in §2.2) for all Reynolds numbers shown, which agrees with Ng & Erlebacher's (1992) secondary instability theory results. The reason why the nonlinear distortion of the primary wave does not appear to influence the secondary (1, 1) mode lies in the fact that the secondary instability resides above the outer peak in the primary mode and not near the wall where nonlinear distortion is most evident.

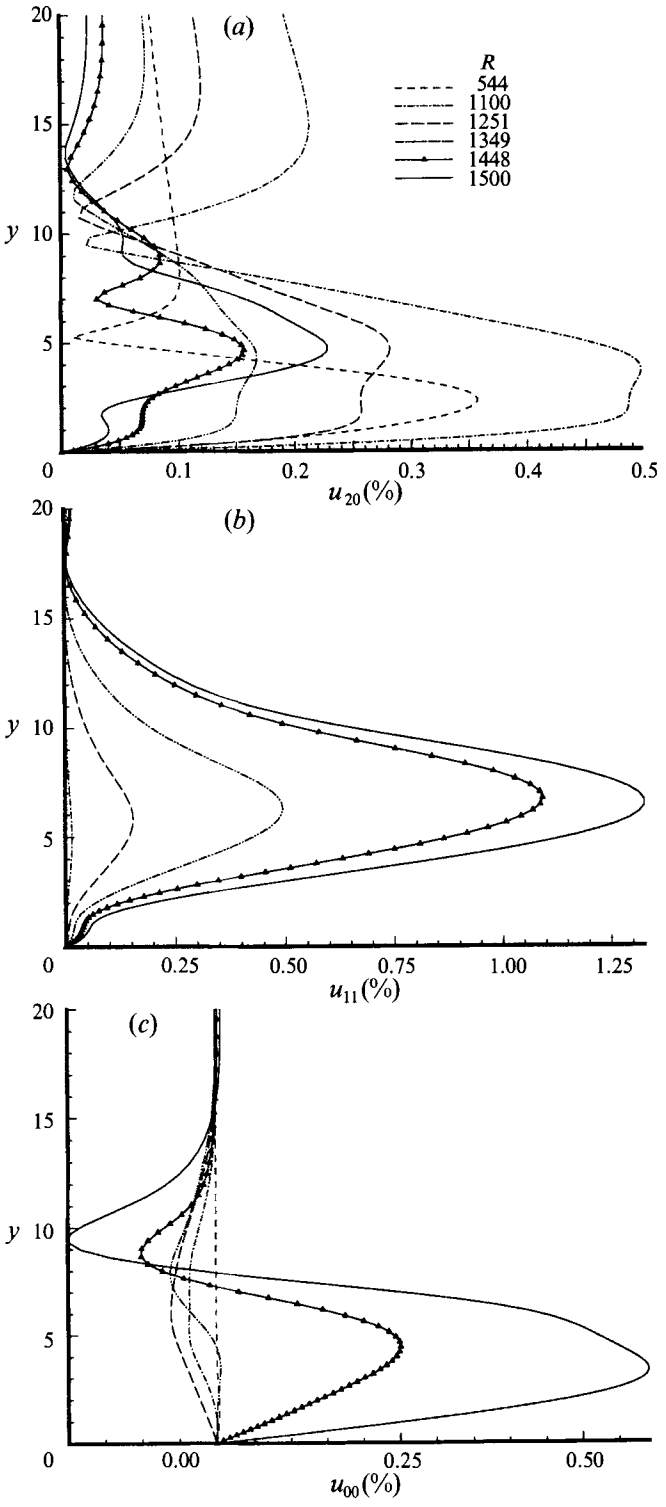

FIGURE 9. Shape function profiles at various Reynolds numbers: (*a*) primary two-dimensional wave (2, 0), (*b*) subharmonic wave (1, 1), (*c*) mean-flow distortion (0, 0).

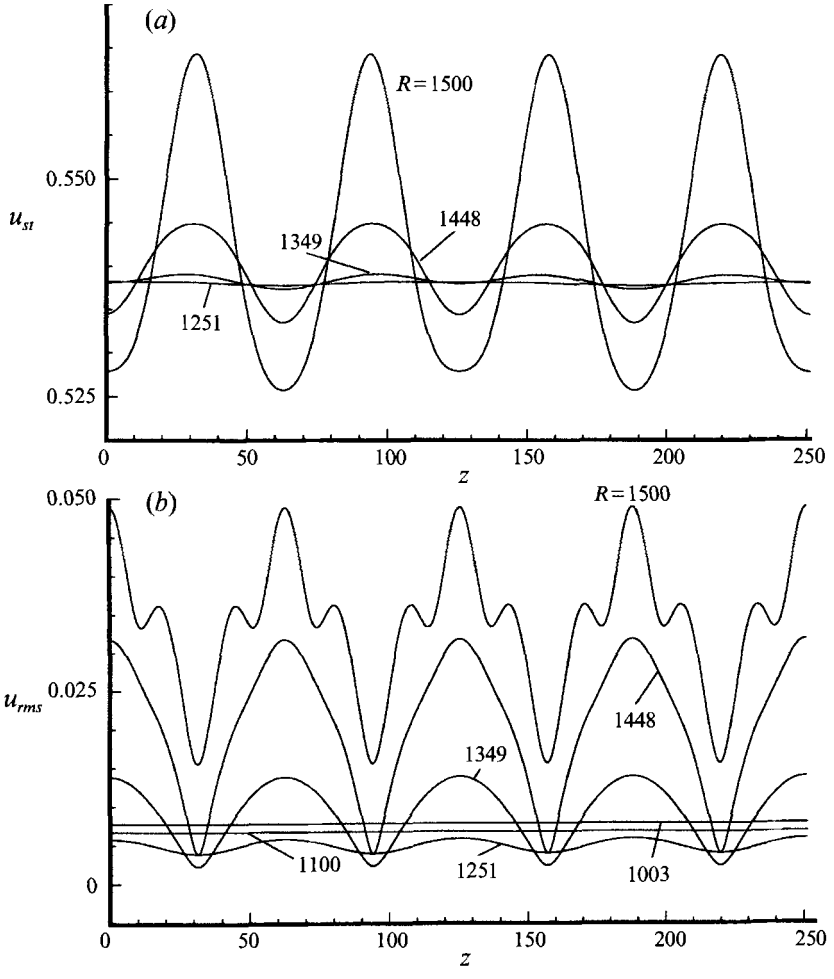

FIGURE 10. Mean and r.m.s. u-velocity distribution at various downstream locations along the spanwise coordinate at $y^*/l_x = 2.3$: (a) mean value, (b) r.m.s. value.

It is interesting to note that the mean-flow distortion mode (figure 9c) is negative for $R < 1400$. This shows that the energy is being transferred from the mean flow to the instability waves. For $R = 1448$ and above, the MFD mode shows a negative value in the outer part of the boundary layer and a positive near the wall. Thus, energy is being extracted from the mean flow in the outer part where secondary instability structure resides and it is being added to the mean flow near the wall, making the mean flow profile fuller as the flow heads towards transition to turbulence.

Figures 10(a) and 10(b) show the variation of both mean and r.m.s. values of the streamwise velocity at $y^*/l_x = 2.3$ along the spanwise coordinate for various Reynolds numbers. The z-coordinate is normalized by l_0 and two spanwise wavelengths ($\lambda_z = 2\pi/\beta$) are shown. The mean values, u_{st}, defined as

$$u_{st}(x, y, z) = \frac{1}{\tau} \int_0^{\tau} u'(x, y, z, t)\, \mathrm{d}t, \tag{3.4}$$

are obtained (figure 10a) by taking the time average of the instantaneous u velocity; thus, only stationary modes (including mean flow distortion and all streamwise vortex

modes) contribute to it. For small Reynolds numbers, the three-dimensional effect is weak and the mean value is uniform across z (e.g. at $R = 1251$). For a Reynolds number of 1349 and beyond, three-dimensionality becomes important as the streamwise vortex modes gain energy (see figure 6). It is evident from figure 10(*a*) that the (0, 2) streamwise vortex mode dominates (by noting two peaks in one spanwise wavelength λ_z) owing to the interaction of the oblique subharmonic waves. We will later discuss in more detail the oblique mode breakdown mechanism where the primary modes are oblique and such an oblique-mode interaction dominates the transition process.

The r.m.s. values (figure 10*b*) were calculated by taking the root mean square of all travelling Fourier modes (therefore excluding mean flow distortion and vortex modes):

$$u_{rms}(x, y, z) = \left(\frac{1}{\tau}\int_0^{\tau} [u'(x, y, z, t) - u_{st}(x, y, z)]^2 \, \mathrm{d}t\right)^{1/2}. \tag{3.5}$$

As can be seen, u_{rms} decreases from $R = 1003$ to $R = 1251$ because of the decay of the primary two-dimensional wave. For Reynolds numbers $R > 1250$, the subharmonic mode overtakes the primary wave and the level of r.m.s. disturbance amplitude increases accordingly. Comparing figures 10(*a*) and 10(*b*), it is clear (e.g. at $R = 1448$) that the maximum r.m.s. amplitude coincides with the minimum in the mean flow and vice versa. In other words, the travelling modes tend to concentrate in the upwash region of the streamwise vortex mode. This situation is similar to that found in the interaction of travelling and stationary crossflow disturbances in three-dimensional boundary layers (Bippes 1991; Malik, Li & Chang 1994). The basic shape of the r.m.s. velocity distribution in figure 10(*b*) looks quite similar to that found by Corke & Mangano (1989) in the low-speed experiments. At $R = 1500$, the peak u_{rms} reaches about 5% and additional local peaks appear as the higher harmonic waves (e.g. the (2, 2) mode) gain considerable energy. This process of spectral broadening will continue as the flow goes through transition.

For the 0.1% case shown in figure 4(*a*), the initial amplitude of the two-dimensional wave is too small to trigger strong secondary instability for either fundamental or subharmonic modes, each of which has an initial amplitude of 0.001%. If the disturbance environment does not prefer two-dimensional modes, it is likely that both two- and three-dimensional modes would have about the same initial amplitudes. For supersonic flows, since oblique modes grow much faster than the two-dimensional waves, the oblique modes will come to dominate the transition process. In the next section, we discuss this mechanism in some detail.

3.3. *Oblique-mode breakdown*

In the next simulation, we force the flow with only a pair of oblique waves, which we now denote as ((1, 1) and (1, −1)) modes, and no other harmonics are included in the initial conditions. To allow the imposed oblique wave to have a larger linear amplification, we choose a lower frequency of $F = 0.2 \times 10^{-4}$ and a spanwise wavenumber of $\beta/R = \pm 0.83 \times 10^{-4}$, which corresponds to an initial wave angle of about 60° at the starting location near the lower-branch neutral point ($R = 750$). The initial amplitude of the oblique waves is assumed to be 0.1% and nine Fourier modes are kept in both temporal and spanwise directions ($M = N = 9$).

The resulting maximum velocity amplitude evolution is shown in figure 11 for some of the representative modes. Like that of the subharmonic secondary instability, the energy cascade exhibits a staggered or 'checkerboard' pattern, i.e. among two-

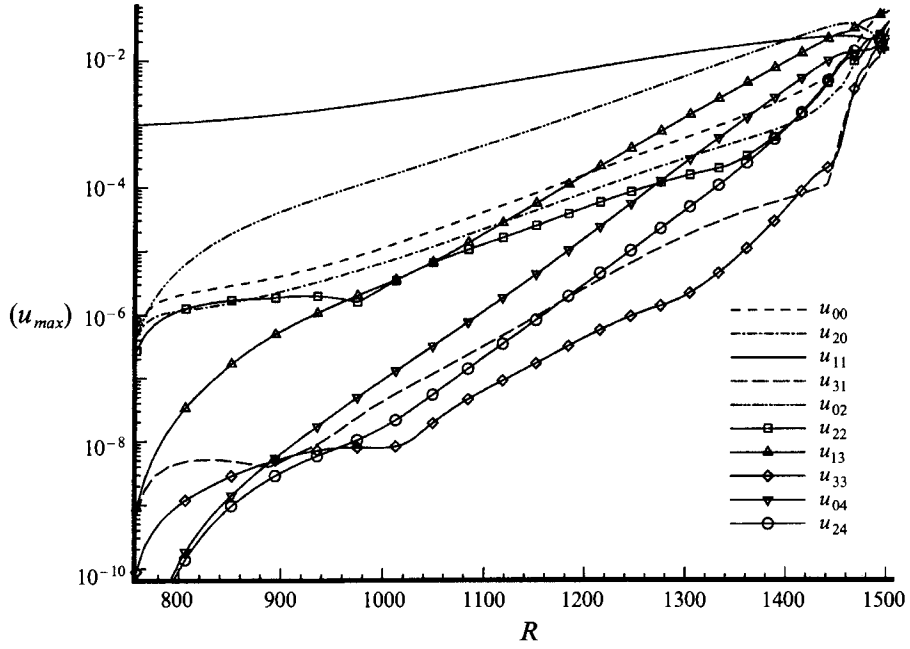

FIGURE 11. Evolution of maximum r.m.s. u-velocity perturbations for the oblique-mode breakdown; $F = 0.2 \times 10^{-4}$ and $\beta/R = 0.83 \times 10^{-4}$.

dimensional modes, only (2, 0), (4, 0), (6, 0), etc. are excited and for 1β modes, only (1, 1), (3, 1), (5, 1), etc. gain energy. The remaining harmonic components (e.g. (1, 0), (3, 0), (0, 1), (2, 1), (2, 3), etc.) are not excited throughout the simulation. The streamwise vortex mode (0, 2) grows very rapidly because of the interaction of the oblique waves ((1, 1)−(1, −1)). Among the active harmonic waves, the (1, 3) mode starts at an amplitude of about 10^{-9} and grows faster than that of the (0, 2) mode, as it gains its energy from the interaction of (1, 1) and (0, 2) modes. Near the end of the calculation, the (1, 3) mode overtakes the already saturated (0, 2) mode. The interaction of these two modes feeds back energy into (1, 1) mode (through (1, 3)−(0, 2)). At this stage, almost all harmonic waves have reached about 1 % (or higher) in amplitude and the flow is transitional (see the wall shear stress plot below).

The crucial mechanism in the above oblique-mode breakdown process is the nonlinear interaction among a wave–vortex triad, i.e. (1, 1), (1, −1) and (0, 2). This triad interaction can be better understood in figure 12 where the amplitudes of both (1, 1) and (0, 2) modes are compared with those from corresponding linear PSE solutions. The linear solution of the vortex mode is obtained by using linear PSE with a prescribed initial condition at $R = 750$. As can be seen, in the nonlinear calculation, the oblique mode is amplified linearly while the vortex mode grows at a much higher rate than its linear counterpart. In the absence of the oblique mode, the vortex mode would have followed the linear solution. The nonlinear forcing of the vortex mode mainly comes from the oblique wave since it is the dominating mode over a long range of x. We note here that the (0, 2) mode is stable according to the classical linear stability theory and the reason why our linear PSE solution in figure 12 shows a region of initial growth (for $R < 1000$) is linked to an 'imperfect' (or non-eigenmode) initial condition which is subject to transient growth, a phenomenon discussed by Schmid & Henningson (1992) for incompressible flow.

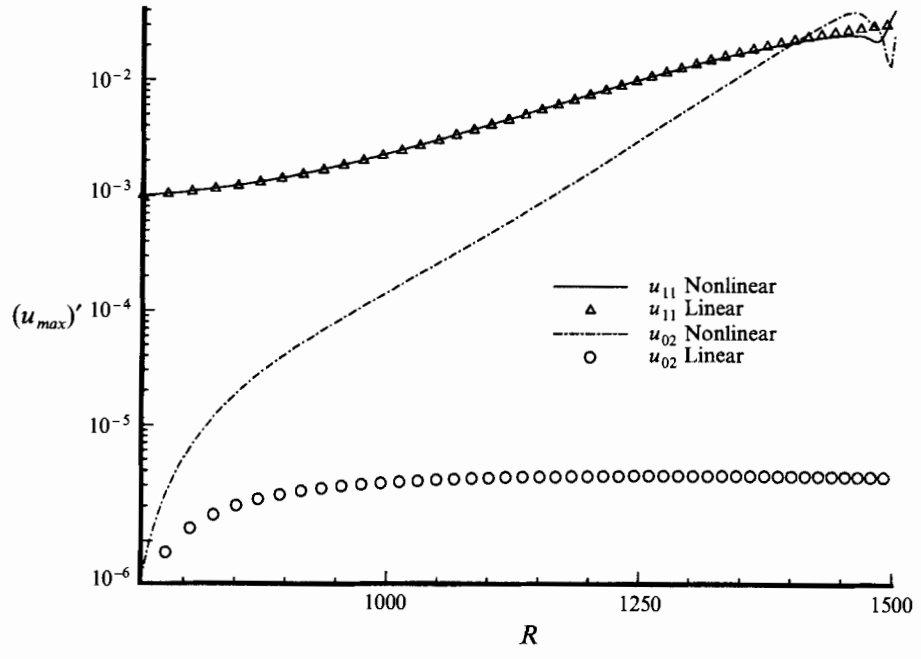

FIGURE 12. Comparison of linear and nonlinear solutions for the wave–vortex triad under an oblique-mode breakdown.

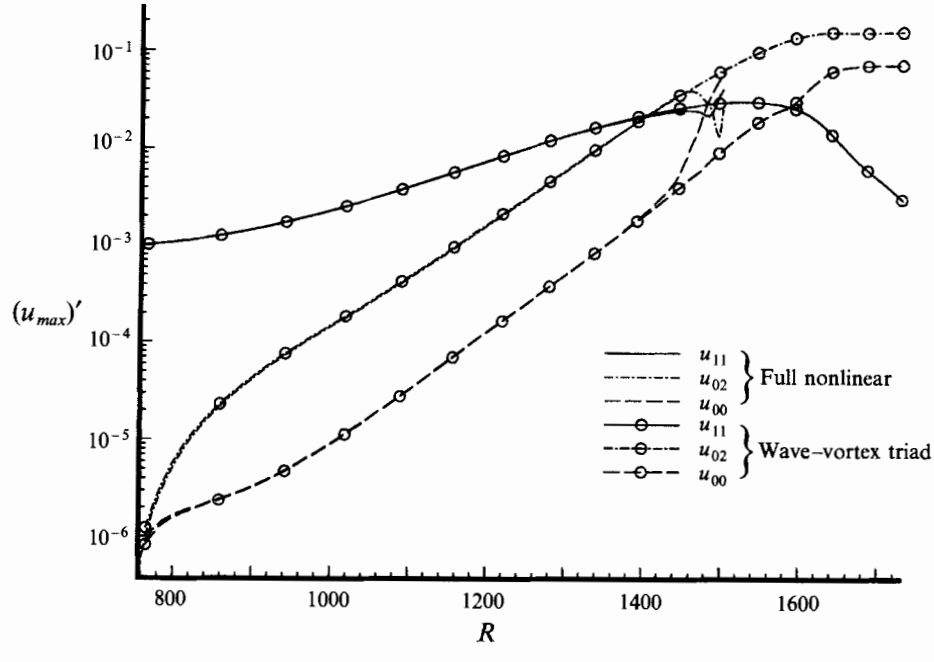

FIGURE 13. Comparison of wave–vortex triad and full nonlinear solutions under an oblique-mode breakdown.

The above results also indicate that the wave–vortex triad interaction is a combination of both linear and nonlinear processes. The oblique modes (1, 1) and (1, −1) grow linearly, while the growth of the vortex mode is mainly due to nonlinear forcing from the oblique wave and the linear transient effect only plays a minor role.

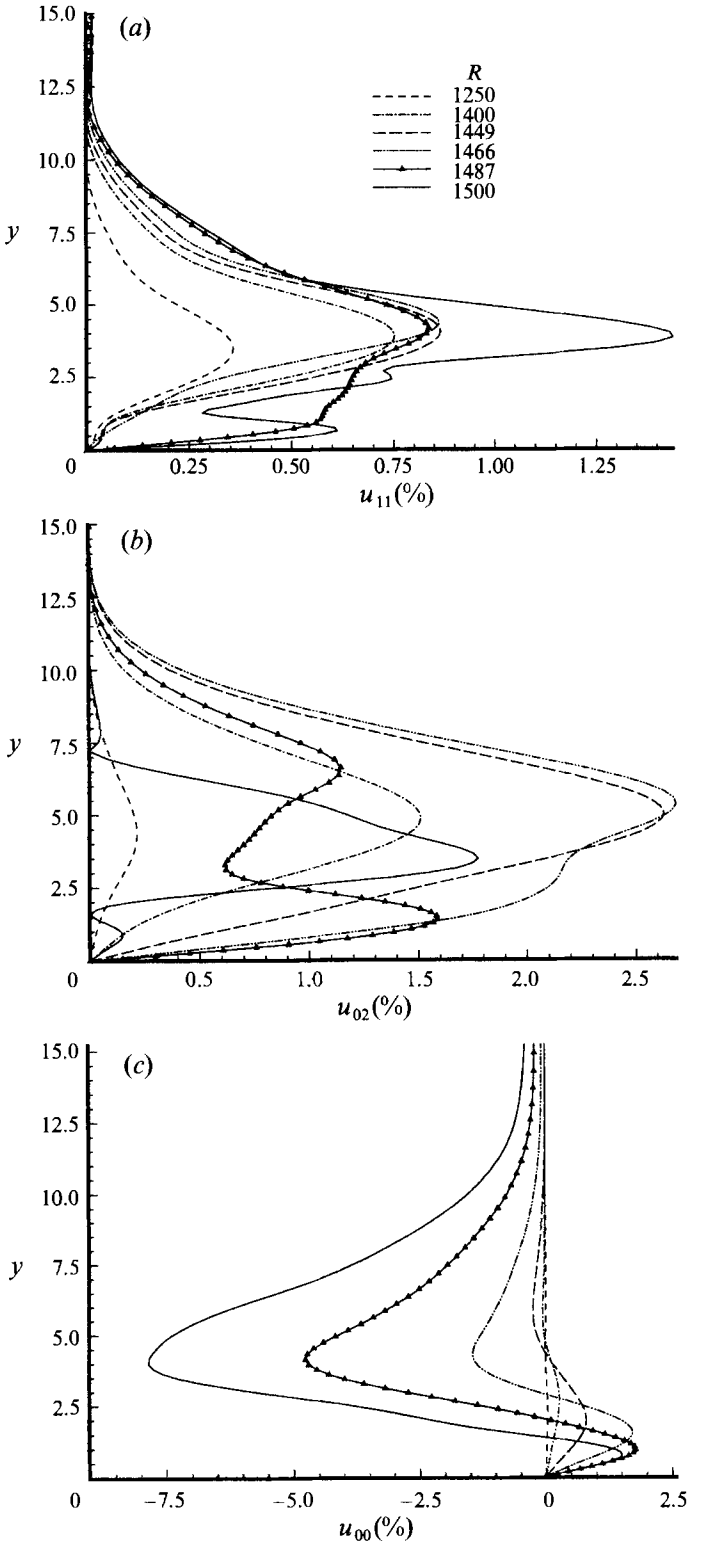

FIGURE 14. Shape-function profiles at various Reynolds numbers under an oblique-mode breakdown: (*a*) primary oblique wave (1, 1), (*b*) streamwise vortex mode (0, 2), (*c*) mean-flow distortion (0, 0).

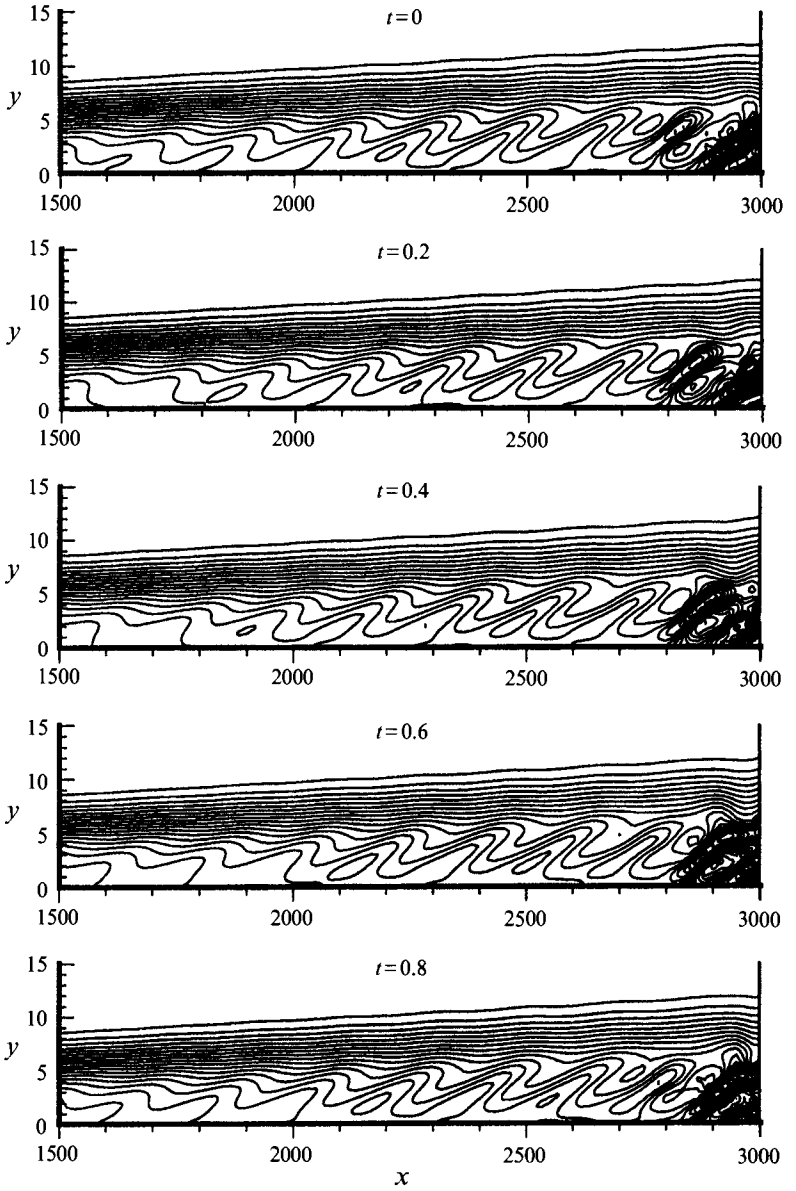

FIGURE 15. Time sequence of spanwise vorticity contours under an oblique-mode breakdown, showing contours in the (x, y)-plane at $z = 0$ (valley plane).

However, surface curvature could appreciably affect the linear mechanism by either suppressing (convex curvature) or enhancing (concave curvature) the growth of the vortex mode. In figure 13, we compare full nonlinear solutions to a simplified nonlinear calculation obtained by keeping only the wave triad and the mean flow distortion in the Fourier series (equation (2.12)) and the remaining harmonic waves are artificially set to zero. It clearly shows that such a simplified triad interaction produces results that agree with those from full nonlinear calculations. Only towards the end of the full nonlinear calculation when other harmonic waves such as (1, 3), (2, 0) etc. reach large amplitudes, does the full nonlinear solution depart from the simplified triad analysis. This departure can be attributed to the nonlinear effect of the vortex mode and the

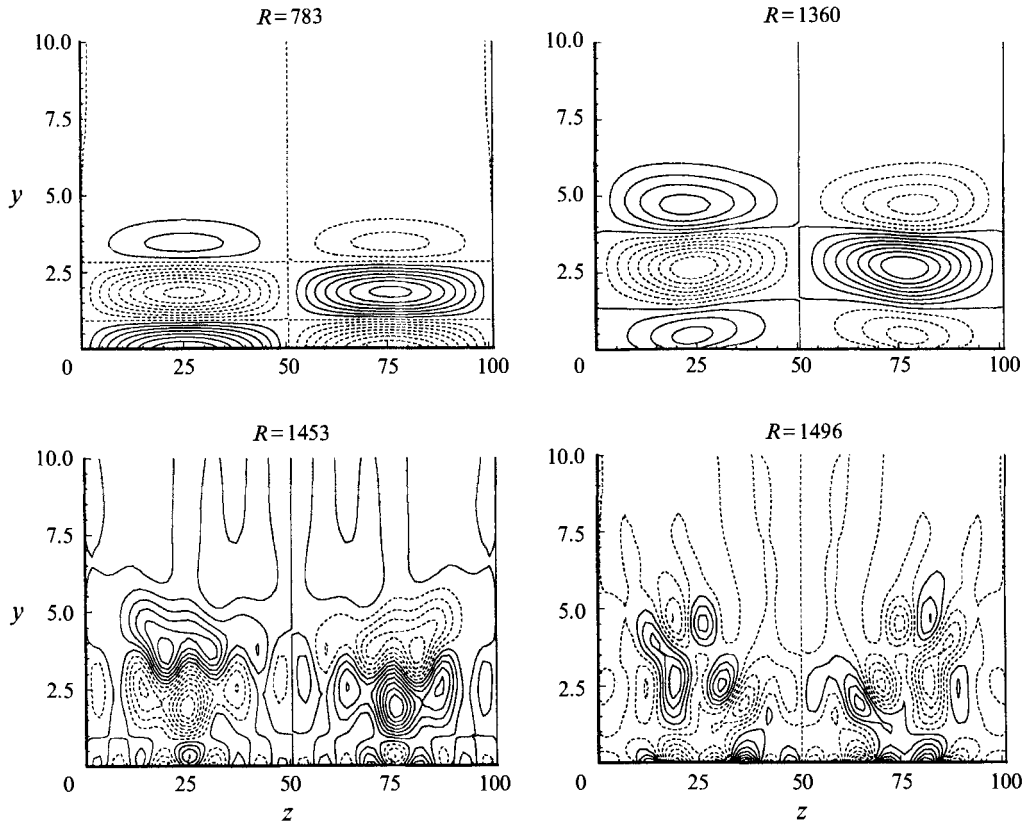

FIGURE 16. Instantaneous streamwise vorticity contours in the (y, z)-plane at various downstream locations.

growth of the (1, 3) mode. Without considering all harmonic components other than the triad, the streamwise vortex mode (0, 2) eventually reaches an equilibrium state with about 10% amplitude. These results suggest that a simplified analysis similar to the secondary instability theory can be constructed to describe the underlying mechanism for the oblique-mode breakdown process. However, in the light of the full nonlinear results shown in figure 11, such a simplified theory would become invalid near the transition onset. The wave-triad stage of the oblique-mode breakdown process is also connected to the vortex/wave interaction theory of Hall & Smith (1989, 1991) but we point out that, in the present case, even before the vortex has a chance to substantially alter the mean flow, harmonics such as (1, 3) mode become dominant and need to be accounted for in the analysis.

The evolution of u-velocity shape functions of the triad (1, 1), (0, 2), and the mean-flow distortion is plotted in figures 14(*a*)–(*c*), respectively. Only representative locations in the nonlinear region are shown. For $R < 1450$, the oblique mode grows linearly (see figure 12) and the amplitude function retains its linear shape. The (0, 2) mode peaks at a slightly larger y than the (1, 1) mode, indicating that nonlinear interaction between these two modes takes place slightly off the critical layer where the oblique mode peaks. In this region, the MFD mode is positive near the wall and negative away from the wall, in contrast to the secondary instability case shown in figure 9(*c*) where the MFD mode has all negative values when resonance occurs. At $R = 1450$, the maximum amplitude of the vortex mode reaches about 2.6% while the

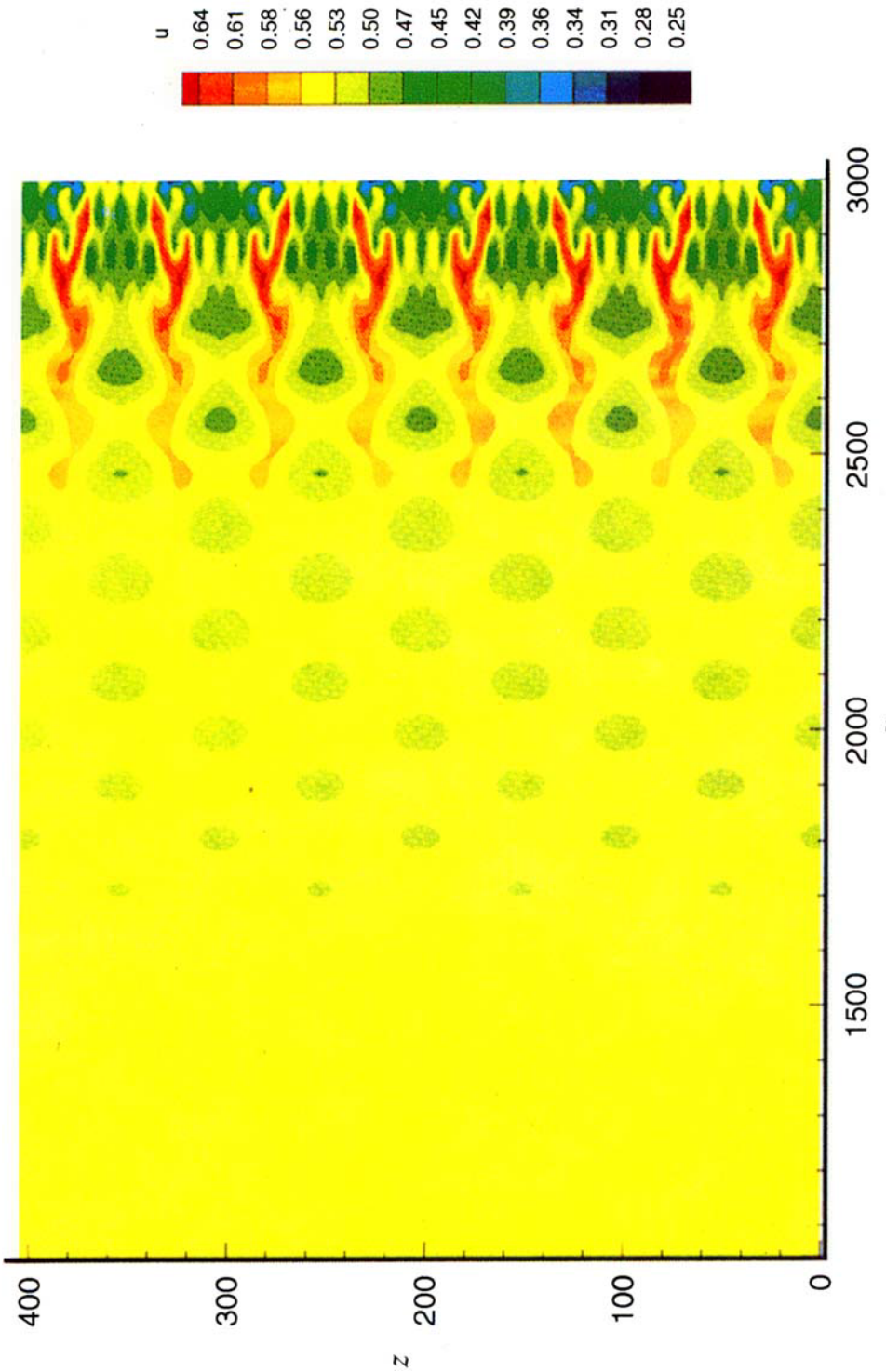

FIGURE 17. Instantaneous u-velocity contours in the (x, z)-plane at $y^*/l_x = 2.3$ for the oblique-mode breakdown case.

MFD mode is less than 1%. This implies that in the linear region of the oblique mode energy exchange between unsteady disturbances and the mean flow is through the vortex mode (0,2) instead of the MFD mode. In the highly nonlinear region ($R > 1450$), both the (1,1) and (0,2) modes change shape rapidly, shown by the appearance of additional local extremums. Furthermore, a large portion of the MFD mode has negative values while the (0,2) mode decays in amplitude. This indicates that the energy exchange in the strongly nonlinear stage is mainly between unsteady disturbances and the MFD mode.

In figure 15 we plot the time sequence of the spanwise vorticity contours in the (x, y)-plane where the r.m.s. wall shear is maximum (valley plane). High shear develops near the end of the simulation for $x > 2700$ where a distinct kink in vorticity distribution is visible. The streamwise vorticity contours in the (y, z)-plane at several downstream locations are shown in figure 16. Initially, the streamwise vorticity contours contain only the dominant oblique wave (at $R = 783$). At $R = 1360$, the amplitude of the (0,2) mode is only slightly lower than that of the (1,1) mode (see figure 11) and therefore the vorticity contour is slightly deformed. In the next two plots, at $R = 1453$ and 1496, many modes have reached amplitudes comparable to the (1,1) mode; consequently, many small structures begin to appear as the flow is becoming transitional. A distinct feature of the oblique-mode breakdown is the early breakup of streamwise vortex: for instance, at $R = 1453$ (corresponding to $x = 2815$ in figure 15), the streamwise vorticity contours show the appearance of small-structure vortices while the region of intense high shear (spanwise vorticity) which often characterizes transition onset is yet to appear (see figure 15). The cause of this rapid vortex breakup is the rather fast spectrum broadening in the spanwise direction associated with the highly amplified (0,2) and (1,3) modes.

Figure 17 (plate 1) depicts the instantaneous streamwise velocity contours in the (x, z)-plane at a wall-normal distance of $y^*/l_x = 2.3$. It shows the oblique-mode breakdown where a high-speed streak (in red) splits into two tips and one of those tips then branches into two. These high – speed regions are engulfed by low-speed regions which also have their own little islands of high-speed regions and the whole pattern gives the impression of a 'fingered' structure extended in the streamwise direction. It should be cautioned here that more Fourier modes may be required to capture the fine details of the flow structure towards the very end of the calculation.

Figures 18(*a*) and 18(*b*) show the mean and r.m.s. u-velocity distributions near the critical layer at $y^*/l_x = 2.3$ (which gives the maximum r.m.s. values) along the spanwise direction for two wavelengths of the oblique mode. At $R = 1250$, the mean flow is almost spanwise-uniform while the u_{rms} distribution shows strong three-dimensionality. At $R = 1400$, the mean flow becomes three-dimensional and the peak u_{rms} increases to about 2%. Note that at $z = 25$ where mean flow has a maximum u_{rms} has a minimum, and that u_{rms} is maximum at $z = 50$ which corresponds to a minimum in the mean flow. At $R = 1449$, the low-speed mean-flow region begins to show oscillations and a new dip appears in the high-speed region at $z = 25$ for $R = 1466$. At $R = 1487$, these oscillations are intensified and the high-speed region at $z = 25$ has become a low-speed region by splitting into two separate high-speed regions, one on either side of $z = 25$. This process continues and at $R = 1500$, the location $z = 25$ (and 75) is now a distinct low-speed region. During this evolution of the mean flow, the peak and valley in the r.m.s. distribution as observed at $R = 1400$ break into additional small-scale peak and valley structure. Near the end of the simulation at $R = 1500$, the peak r.m.s. value has reached about 10%, which is typical in a transitional boundary layer. The results in this highly nonlinear region reveal that strong three-dimensional

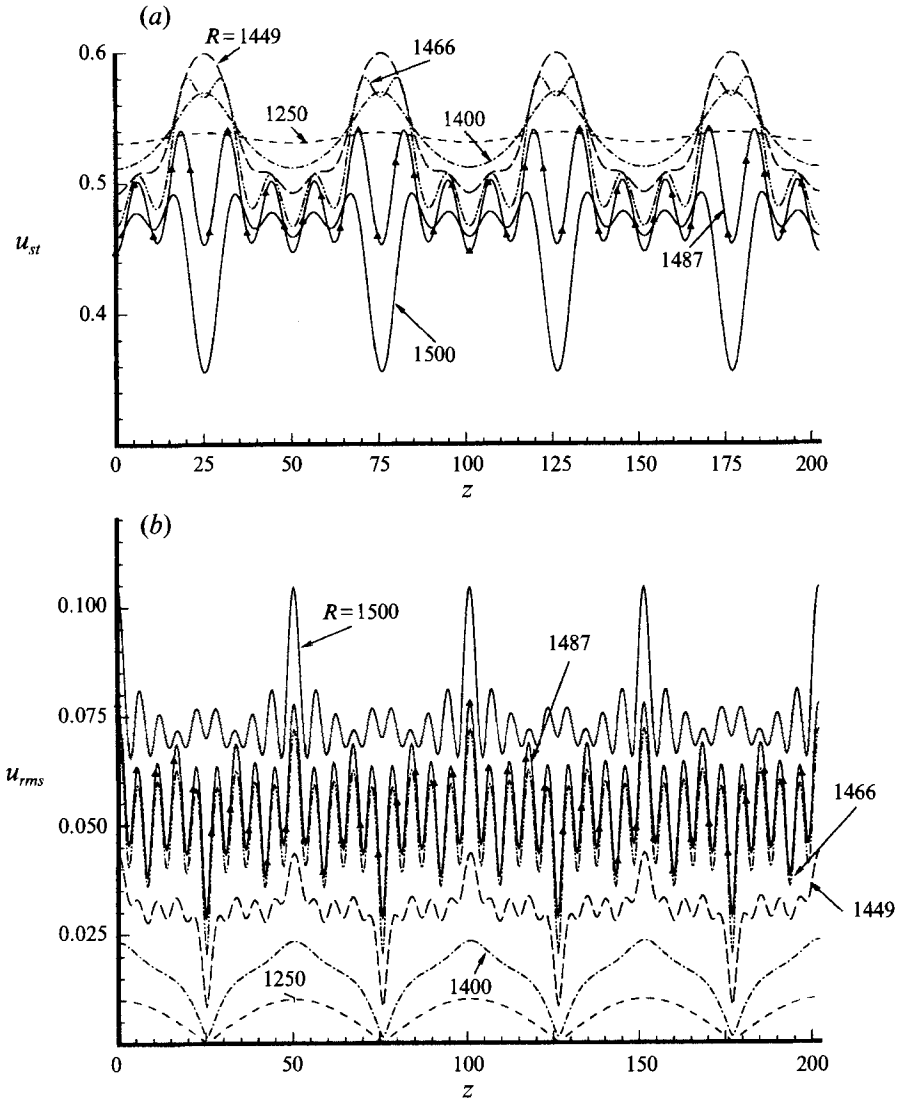

FIGURE 18. Mean and r.m.s. u-velocity distribution along the spanwise coordinate at $y^*/l_x = 2.3$ in the nonlinear region under an oblique-mode breakdown: (*a*) mean value, (*b*) r.m.s. value.

effects appear in both mean and r.m.s. velocities. The large-scale peak–valley structure which characterizes the unstable laminar boundary layer is gradually evolving into a small-scale rapidly oscillating but more uniform structure (between the r.m.s. peaks). At $z = 25$, for example, a distinct minimum in u_{rms} has disappeared owing to the emergence of a low-speed mean-flow region which helps amplify the unsteady disturbances. Following this trend, we expect that both mean and r.m.s. values will eventually reach a uniform state which characterizes the fully developed turbulent boundary layer. At $R = 1449$ which correlates with the rise of wall shear stress (see below), the peak u_{rms} has reached about 4.3%.

To study the flow characteristics in the transition zone, we plot in figure 19 the instantaneous u velocity versus time near the wall (at a height of $y^*/l_x = 0.044$ and $z = 0$ where u_{rms} peaks along the spanwise direction) for various Reynolds numbers

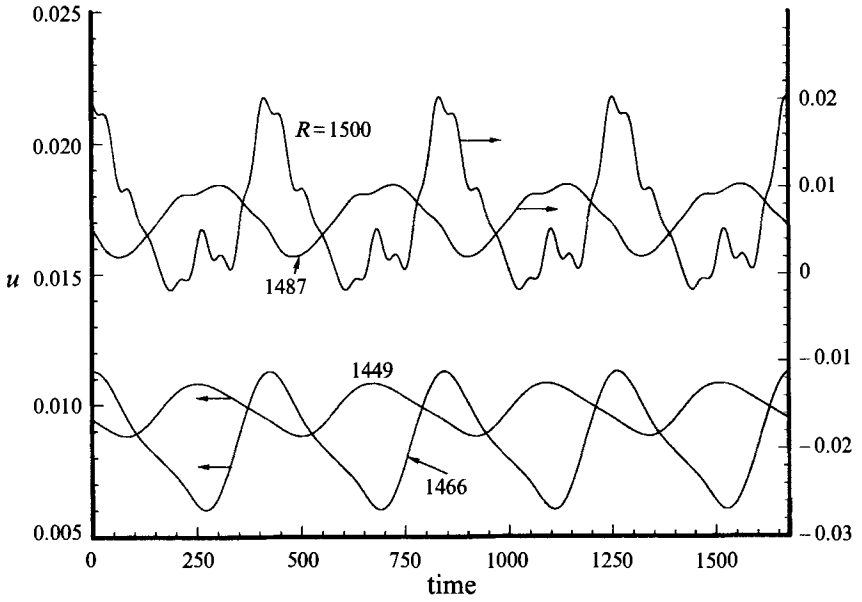

FIGURE 19. Time signal of u velocity near the wall ($y^*/l_x = 0.044, z = 0$) in the nonlinear region of the oblique-mode breakdown.

near the end of simulation. Since the wall u velocity is identically zero for all time, the velocity trace shown in figure 19 also represents the instantaneous wall shear. As can be seen, the time signal at $R = 1449$, 1466, 1487, although being modulated by harmonic waves, shows a dominant frequency of the input oblique wave. However, at $R = 1500$, a 'transition-like' signal is evident with additional high-frequency disturbances riding on the primary disturbance. It is clear that the flow has entered the transition region (see also the mean wall shear distribution given below). Of special interest is the observation that small periods of negative streamwise velocity begin to appear, indicating an instantaneous flow separation in the transition region.

As mentioned above, the staggered energy cascade is a distinct feature of the oblique-mode breakdown process. In 'natural' environments, those off-cascade 'quiet' modes must also be present. In the next calculation, we study the effect of these quiet modes (e.g. (0, 1), (1, 0) etc.) on the oblique-mode breakdown. Figures 20(*a*) and 20(*b*) represent the solution obtained by forcing one of the quiet modes, (1, 0) (with an amplitude of 0.1%), in addition to the oblique modes $(1, \pm 1)$ (through nonlinear interaction all other quiet modes would be excited). Comparing figure 20(*a*) with figure 11, one finds that all harmonic waves within the staggered cascade evolve essentially in a similar fashion for both calculations. The location of spectrum broadening occurs at about the same Reynolds number (around $R = 1500$). The evolution of some of the quiet modes is shown in figure 20(*b*). The presence of the (1, 0) mode has triggered the growth of many other harmonic waves. The most important ones are listed below:

$$(0,1) = (1,1) + (-1,0),$$
$$(1,2) = (1,1) + (0,1),$$
$$(0,3) = (0,2) + (0,1),$$
$$(2,3) = (1,3) + (1,0),$$
$$(1,4) = (1,3) + (0,1).$$

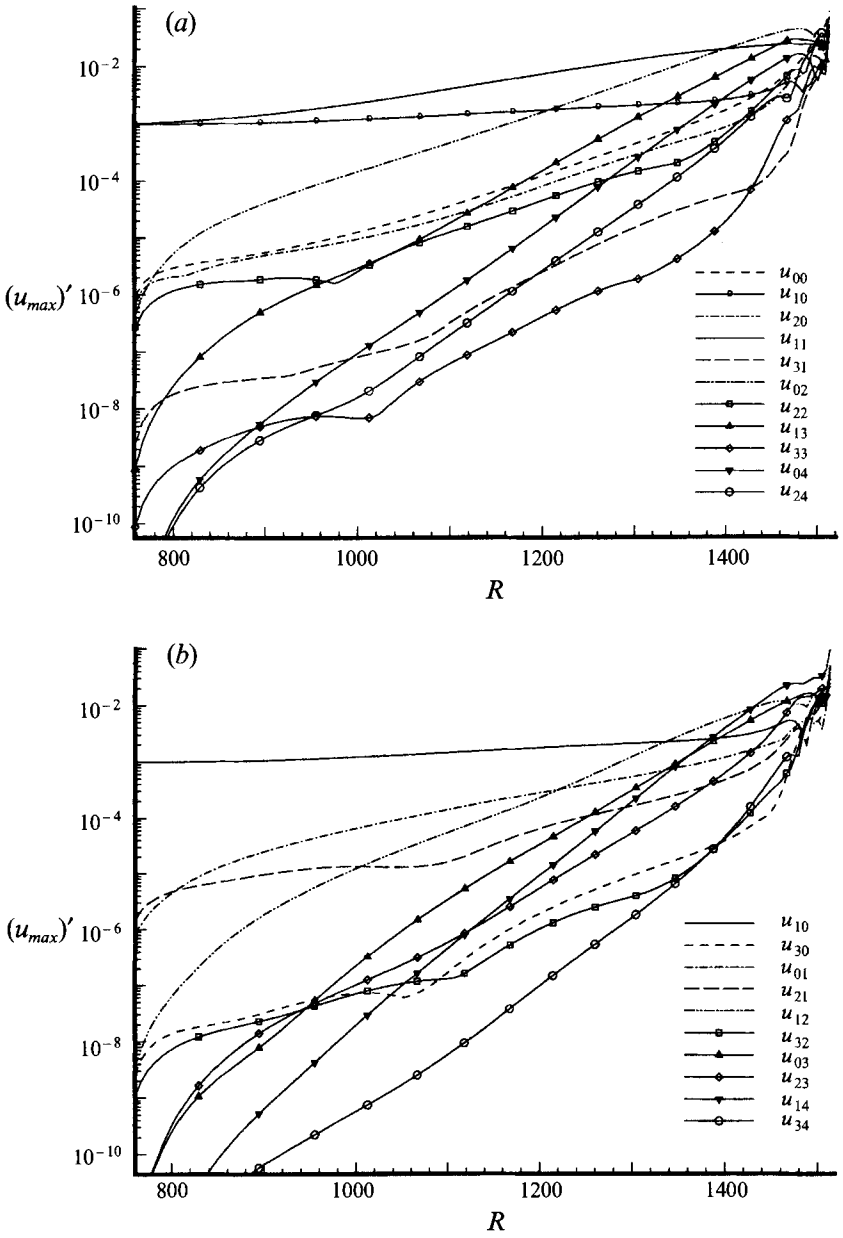

FIGURE 20. Evolution of maximum r.m.s. u-velocity perturbations for various Fourier modes for the oblique-mode breakdown with the addition of the (1, 0) mode: (*a*) staggered cascade modes, (*b*) off-cascade quiet modes.

In order to further examine the effect of (1, 0) forcing, we compare in figure 21 the evolution of some of the important modes (1, 1), (0, 2) and (0, 0) with and without the (1, 0) mode in the initial conditions. It clearly shows that the two-dimensional mode (1, 0) does not affect either the oblique or the streamwise vortex mode over a wide range of Reynolds numbers. However, the amplitude of the mean-flow distortion is higher owing to the additional contribution from the now-active quiet modes but the excess lasts only up to about $R = 1250$.

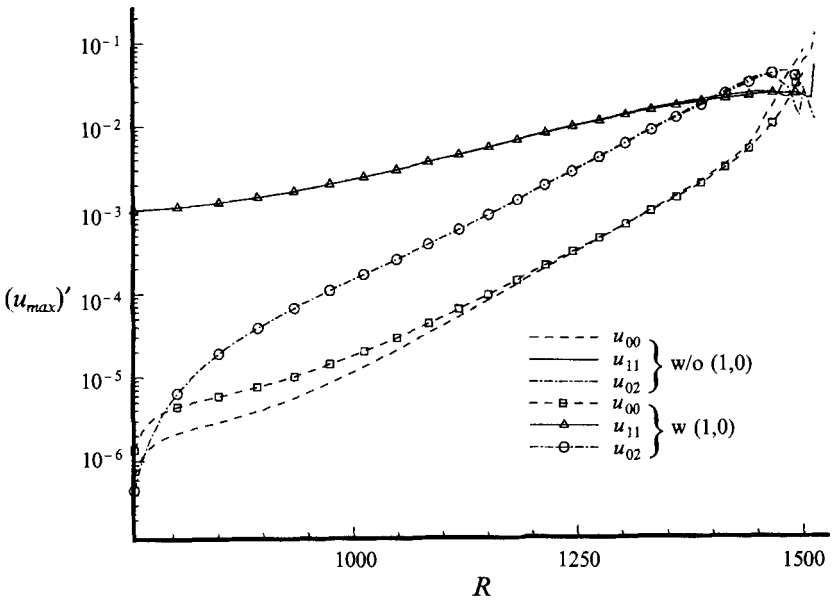

FIGURE 21. Comparison of the evolution of the triad and MFD modes under an oblique-mode breakdown with or without the addition of the (1,0) mode.

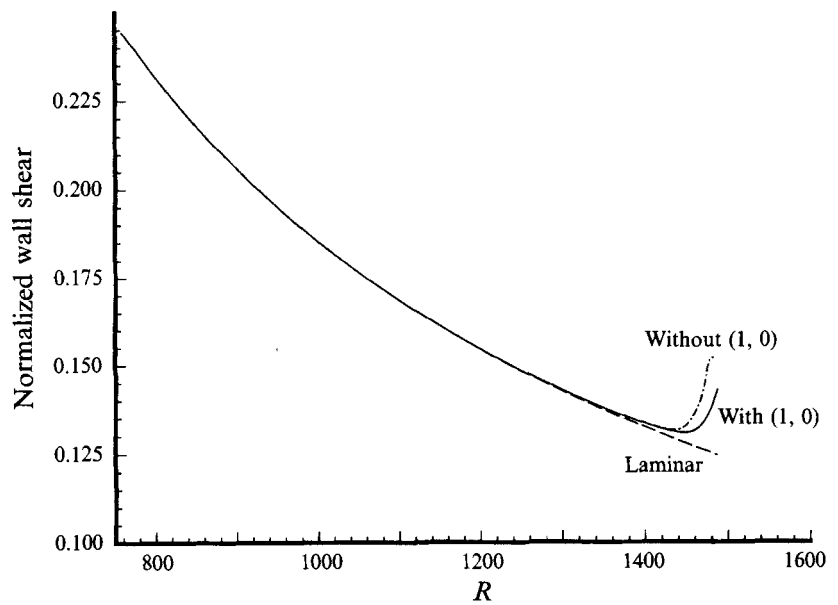

FIGURE 22. Average wall shear versus Reynolds numbers for the oblique-mode breakdown with or without the addition of the (1,0) mode.

For $R > 1450$, we begin to see some visible differences, *vis-à-vis* oblique modes and streamwise vortices, between the two calculations owing to the presence of the energetic quiet modes. We plot the average wall shear versus Reynolds number for both cases in figure 22. As expected, for the onset of transition (where wall shear rises) they differ only slightly from each other. In either case, transition takes place roughly

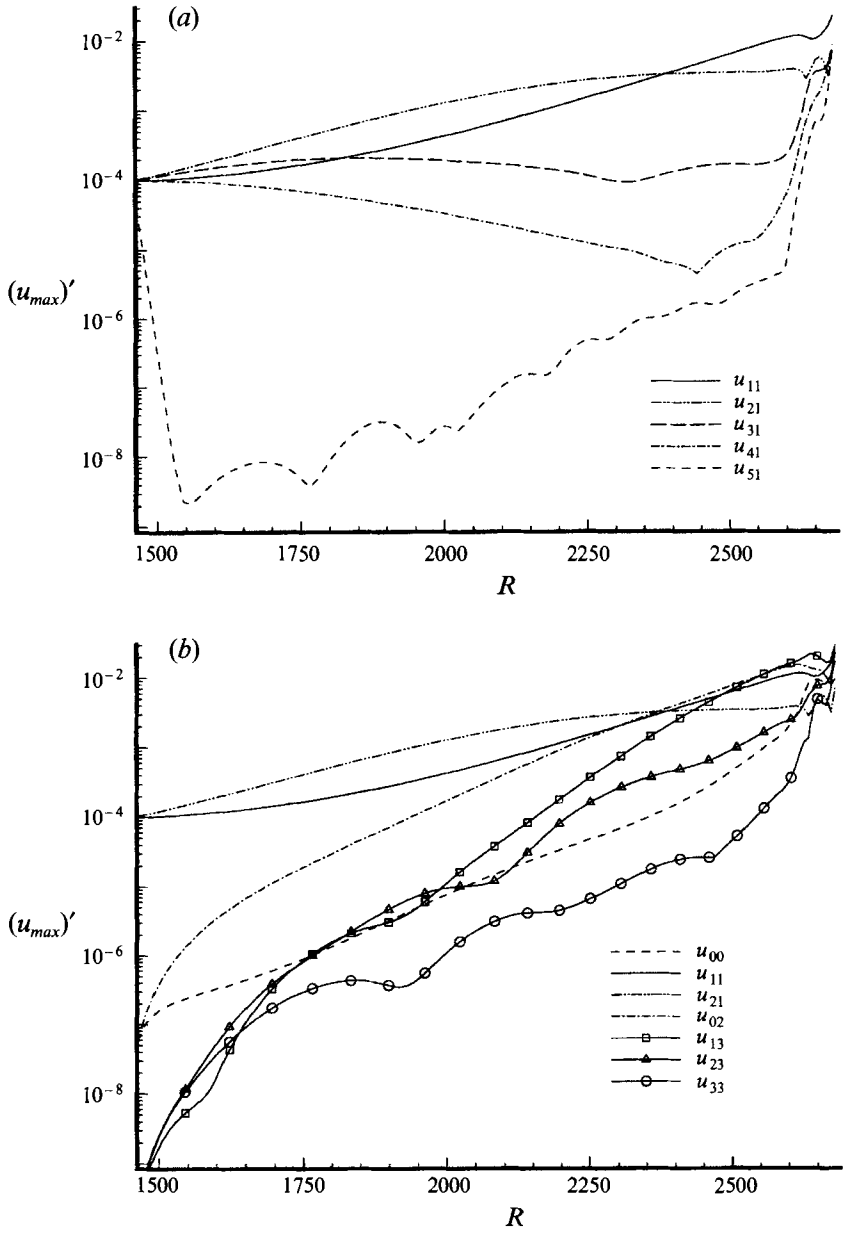

FIGURE 23. Evolution of maximum r.m.s. u-velocity perturbations for multiple oblique-mode interaction: (*a*) forced multiple oblique modes, (*b*) representative Fourier modes.

at a Reynolds number of about 1450. This is equivalent to a length Reynolds number of about 2.1×10^6, which is within the range measured in conventional supersonic wind tunnels.

3.4. *Multiple oblique-mode interaction*

The oblique-mode breakdown calculations discussed above were performed by forcing with only one pair of oblique waves. It would be of interest to study nonlinear interaction of multiple (frequency) oblique waves since, in general, oblique waves with various frequencies would be present in the natural environment.

In this calculation, five pairs of oblique modes with an equal amplitude of 0.01 % are forced at $R = 1450$. They are $(1, \pm 1)$, $(2, \pm 1)$, $(3, \pm 1)$, $(4, \pm 1)$ and $(5, \pm 1)$, corresponding to frequencies F of 0.06×10^{-4}, 0.12×10^{-4}, 0.18×10^{-4}, 0.24×10^{-4} and 0.30×10^{-4}, respectively. The spanwise wavenumber is chosen to be $\beta/R = 0.25 \times 10^{-4}$ corresponding to a wave angle of about 58° at $R = 1450$ (the lower-branch neutral point). Nine temporal and spanwise Fourier modes are used in the calculation. The computed evolution of r.m.s. u-velocity amplitude is presented in figures 23(*a*) and 23(*b*). In figure 23(*a*), we show the amplitudes of the five forced oblique modes. At the starting location $R = 1450$, the two high-frequency modes, (4, 1) and (5, 1), have already passed their linear upper-branch neutral points (see figure 2) and are damped right from the beginning. The remaining three modes essentially evolve linearly until the streamwise vortex mode (0, 2) grows to sufficiently large amplitude. Both (2, 1) and (3, 1) reach the upper-branch neutral location earlier than the (1, 1) mode. Consequently, the (1, 1) mode becomes the dominant disturbance for $R > 2400$. The evolution of all five modes essentially follows a linear trend over a long distance downstream because the initial amplitude is quite low (0.01 %) for all five modes.

In figure 23(*b*), we plot the amplitudes of two dominant modes (1, 1) and (2, 1), together with some of the important harmonics. The nonlinear interaction of each pair of oblique waves would contribute to the growth of the streamwise vortex mode (0, 2). As can be seen, the (0, 2) mode overtakes both the (1, 1) and (2, 1) modes at around $R = 2400$. Also shown in the figure are three harmonic modes (1, 3), (2, 3) and (3, 3). Among these, the (1, 3) mode becomes the dominant instability towards the end of the calculation. This implies that although the (2, 1) mode dominates initially, the mechanism which eventually leads to transition is the instability associated with the interaction of the (0, 2) and (1, 1) modes. In a low-disturbance environment, all instability waves would begin with quite small amplitudes and evolve linearly. The instability wave with the largest linear amplification will eventually dominate (such as the (1, 1) mode shown above) and the breakdown would be associated with the instabilities triggered by this most-amplified mode and the streamwise vortex, as we have demonstrated in the above example. Of course, the initial amplitude of the oblique waves plays a crucial role and must be determined based upon receptivity calculations.

We compare the above multiple-mode results with those from keeping only one primary mode (the (1, 1) mode) in figure 24. It clearly shows that the presence of higher frequency oblique modes does not affect the (1, 1) mode itself, since this mode evolves linearly over a long distance downstream. However, since each high-frequency primary oblique mode adds an additional contribution to the streamwise vortex mode through nonlinear interaction, the (0, 2) mode starts with a much higher initial amplitude as compared to the single-mode case. As a result, the initial level of the amplitude of the (1, 3) mode is about two orders of magnitude higher in the multiple-mode case. The growth rates of the (0, 2) and (1, 3) modes are about the same for both cases. Since the multiple-mode case starts with much higher initial amplitudes, strong nonlinear interaction and transition onset occur earlier than for the single-mode case. Based upon the skin-friction rise, transition onset for the former case occurs at $R = 2600$, as compared to $R = 2750$ for the latter case.

Nonlinear PSE results in §3.3 indicate that the oblique-wave interaction can lead to breakdown to turbulence with a relatively low initial amplitude compared to the secondary mechanism. Low-frequency oblique waves would require a much lower initial amplitude for breakdown owing to large growth via linear mechanism. To show this, we compute the oblique-wave breakdown process with various initial amplitudes

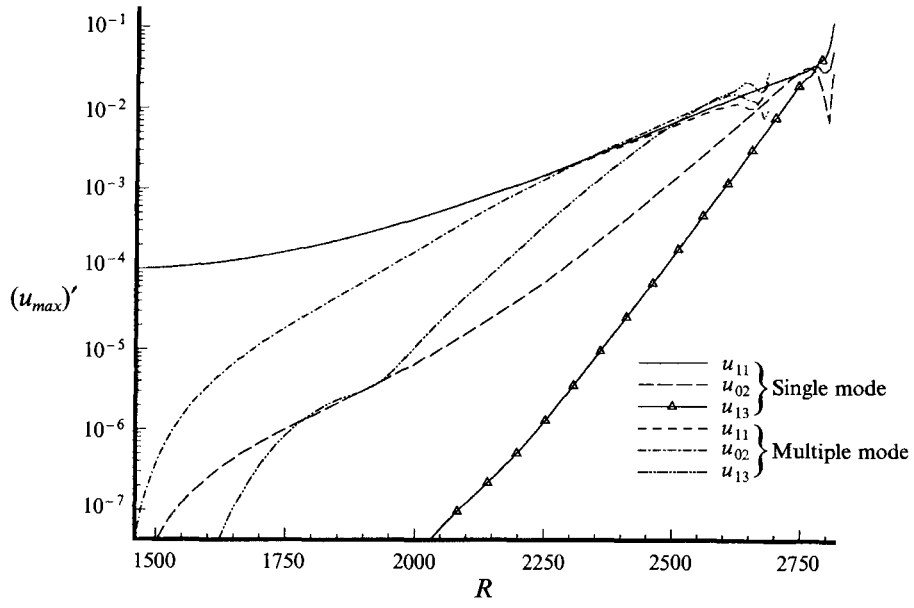

FIGURE 24. Comparison of single and multiple oblique-mode interaction for the triad and secondary instability modes.

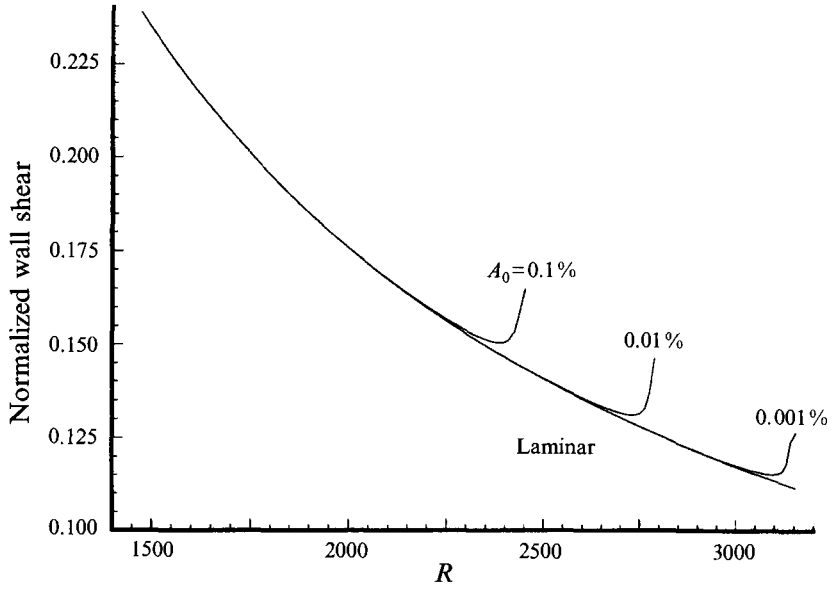

FIGURE 25. Average wall shear versus Reynolds numbers for various initial amplitudes of the oblique-mode breakdown; $F = 0.06 \times 10^{-4}$ and $\beta/R = 0.25 \times 10^{-4}$.

for a disturbance frequency of 0.06×10^{-4} (from linear theory, this frequency is amplified by almost 5000 times between the lower and upper neutral point for $\beta/R = 0.25 \times 10^{-4}$). The variation of wall shear with Reynolds number for various initial amplitudes is shown in figure 25. Transition Reynolds numbers (the rise of wall shear) are found to be around 2450, 2800 and 3150 for initial amplitudes of 0.1%, 0.01% and 0.001%, respectively. We note here that the corresponding logarithmic amplitude factors (equation (3.1)) based upon quasi-parallel linear theory at transition

are 3.8, 5.8 and 7.4, respectively. Comparison with figure 22 shows that if the initial amplitude is 0.1% both for $F = 0.2 \times 10^{-4}$ and $F = 0.06 \times 10^{-4}$, the former will lead to transition first at $R = 1450$ which is close to the neutral location for the latter. Additional calculations with an initial amplitude of 0.0001% show that the primary oblique waves together with their harmonics eventually saturate and transition does not occur. A disturbance with frequency lower than 0.06×10^{-4} may lead to transition for an initial amplitude of 0.0001%. In fact, additional calculations were performed for a Mach 3.5 boundary layer for which transition data were available from Chen *et al.* (1989) who found that transition occurred at $R \approx 3500$ in the 'quiet' environment and $R \approx 1600$ with high levels of free-stream disturbances. PSE calculations with an initial amplitude of about 0.0001% yielded transition Reynolds number quite close to 3500.

4. Conclusions

Nonlinear PSE is used to study two transition mechanisms in low-supersonic flat-plate boundary layers. As in incompressible flow, secondary instability under a two-dimensional primary disturbance can also lead to breakdown to turbulence in supersonic flows. Qualitatively, this mechanism reveals similar behaviour in compressible cases as in incompressible ones. The main difference is that the initial amplitude (of the primary wave) required for transition onset is higher in compressible flows.

The second mechanism investigated is the oblique-mode breakdown. This mechanism involves a pair of oblique first-mode waves with an equal but opposite wave angle to the mean flow direction. Nonlinear interaction of these two waves produces a streamwise vortex. It is shown that the oblique waves and streamwise vortex constitute a nonlinear triad interaction which causes the vortex to grow at a rate much faster than the oblique waves, which are amplified linearly. The interaction of the vortex ((0, 2) mode) and the oblique ((1, 1) mode) modes give rise to other harmonics (e.g. (1, 3) mode) and the flow becomes transitional. This oblique mode breakdown also constitutes the second stage of the breakdown in the secondary instability mechanism where the oblique subharmonics reach sufficient amplitude and their mutual interaction produces a streamwise vortex. From then on, the interaction of these subharmonics and the vortex will produce a transition scenario discussed here for the oblique-mode mechanism.

Both transition mechanisms are studied at Mach 1.6 by varying the initial amplitudes of various two- and three-dimensional first-mode waves. When the two-dimensional wave has an initial amplitude on the order of 0.5% or higher (and three-dimensional waves have much lower amplitudes), the secondary instability mechanism is more likely to occur. Conversely, when the two-dimensional wave has a lower amplitude and the amplitude of the three-dimensional wave exceeds a threshold value (which depends on the frequency), oblique-mode breakdown prevails. Since most amplified first-mode waves in supersonic flows are three-dimensional, the oblique-wave breakdown mechanism appears to be a more likely route to transition (see Goldstein 1990) than the traditional secondary instability mechanisms which are often present in incompressible boundary layers in a low-disturbance environment.

Vorticity structures and instantaneous velocity signals are examined for the oblique-mode breakdown. The results suggest that a rapid spectrum broadening in the spanwise direction results in the early appearance of small-scale streamwise vortical structures. The energy cascade under an oblique-mode breakdown reveals a staggered pattern. The off-cascade modes have very little effect on the breakdown process.

Computed instantaneous velocity signals near the wall show that regions of negative wall shear are present in the breakdown stage, indicating an unsteady flow separation. Nonlinear PSE calculations also suggest that an initial disturbance amplitude of about 0.1% leads to transition Reynolds numbers found commonly in conventional supersonic wind tunnels. Calculations also indicate that for transition Reynolds numbers obtainable in flight and 'quiet' supersonic wind tunnels, the initial disturbance amplitude in the boundary layer must be very small, of $O(0.001\,\%)$ or even lower, if the oblique-mode breakdown is active.

This work was sponsored by Theoretical Flow Physics Branch, NASA Langley Research Center under NASA Contract NAS1-19299. The authors appreciate the encouragement and support provided by Drs Ajay Kumar and Craig Streett.

REFERENCES

BERTOLOTTI, F. P. & HERBERT, TH. 1991 Analysis of the linear stability of compressible boundary layers using the PSE. *J. Theoret. Comput. Fluid Mech.* **3**, 117–124.

BERTOLOTTI, F. P., HERBERT, TH. & SPALART, P. R. 1992 Linear and nonlinear stability of the Blasius boundary layer. *J. Fluid Mech.* **242**, 441–474.

BESTEK, H., THUMM, A. & FASEL, H. 1992 Direct numerical simulation of three-dimensional breakdown to turbulence in compressible boundary layers. *13th Intl Conf. Num. Meth. Fluid Dyn., Rome, July 6–10.*

BIPPES, H. 1991 Experiments on transition in three-dimensional accelerated boundary layer flows. *R. Aeronaut. Soc. Conf. on Boundary Layer Transition and Control, Cambridge, UK.*

CHANG, C.-L. & MALIK, M. R. 1992 Oblique mode breakdown in a supersonic boundary layer using nonlinear PSE. In *Instability, Transition and Turbulence* (ed. M. Y. Hussaini, A. Kumar & C. L. Streett), pp. 231–241. Springer.

CHANG, C.-L. & MALIK, M. R. 1993 Non-parallel stability of compressible boundary layers. *AIAA Paper* 93-2912.

CHANG, C.-L., MALIK, M. R., ERLEBACHER, G. & HUSSAINI, M. Y. 1991 Compressible stability of growing boundary layers using parabolized stability equations. *AIAA Paper* 91-1636.

CHANG, C.-L., MALIK, M. R. & HUSSAINI, M. Y. 1990 Effects of shock on the stability of hypersonic boundary layers. *AIAA Paper* 90-1448.

CHEN, F.-J., MALIK, M. R. & BECKWITH, I. E. 1989 Boundary-layer transition on a cone and flat plate at Mach 3.5. *AIAA J.* **27**, 687–693.

CHOUDHARI, M. & STREETT, C. L. 1993 Interaction of a high-speed boundary layer with unsteady free-stream disturbances. In *Symp. on Transitional and Turbulent Compressible Flows, ASME Fluids Eng. Conf., Washington, D.C., June 20–23.*

CORKE, T. C. 1989 Effect of controlled resonant interactions and mode detuning on turbulent transition in boundary layers. In *Proc. IUTAM Symp. on Laminar-Turbulent Transition, Toulouse, France* (ed. D. Arnal & R. Michel).

CORKE, T. C. & MANGANO, R. A. 1989 Resonant growth of three-dimensional modes in transitioning Blasius boundary layers. *J. Fluid Mech.* **209**, 93–150.

CRAIK, A. D. D. 1971 Nonlinear resonant instability in boundary layers. *J. Fluid Mech.* **50**, 393–413.

DEMETRIADES, A. 1989 Growth of disturbances in a laminar boundary layer at Mach 3. *Phys. Fluids* A **1**, 312–317.

EL-HADY, N. M. 1992 Secondary instability of high-speed flows and the influence of wall cooling and suction. *Phys. Fluids* A **4**, 727–743.

ERLEBACHER, G. & HUSSAINI, M. Y. 1990 Numerical experiments in supersonic boundary-layer stability. *Phys. Fluids* A **2**, 94–104.

FASEL, H. F., RIST, U. & KONZELMANN, U. 1990 Numerical investigation of three-dimensional development in boundary-layer transition. *AIAA J.* **28**, 29–37.

FEDOROV, A. V. & KHOKHOLV, A. P. 1991 Excitation of unstable modes in a supersonic boundary layer by acoustic waves. *Izv. Akad. Nauk SSSR, Mekh. Zhidk. Gaze*, 67–74.

FEDOROV, A. V. & KHOKHOLV, A. P. 1992 Sensitivity of a supersonic boundary layer to acoustic disturbances. *Izv. Akad. Nauk SSSR, Mekh. Zhidk. Gaza*, 40–47.

GOLDSTEIN, M. E. 1990 Position paper for the panel on theory. In *Instability and Transition*, vol. I (ed. M. Y. Hussaini & R. G. Vogt), pp. 6–10. Springer.

GOLDSTEIN, M. E. & CHOI, S.-W. 1989 Nonlinear evolution of interacting oblique waves on two-dimensional shear layers. *J. Fluid Mech.* **207**, 97–120.

HALL, P. & SMITH, F. T. 1989 Nonlinear Tollmien–Schlichting/vortex interaction in boundary layers. *Euro. J. Mech.* B/*Fluids* **8**, 179.

HALL, P. & SMITH, F. T. 1991 On strongly nonlinear vortex/wave interactions in boundary-layer transition. *J. Fluid Mech.* **227**, 641.

HAYES, W. D. & PROBSTEIN, R. F. 1959 *Hypersonic Flow Theory*. Academic.

HERBERT, TH. 1983 Secondary instability of plane channel flow. *Phys. Fluids* **26**, 871.

HERBERT, TH. 1988 Secondary instability of boundary layers. *Ann. Rev. Fluid Mech.* **20**, 487.

HERBERT, TH. 1991 Boundary-layer transition – analysis and prediction revisited. *AIAA Paper* 91-0737.

JOSLIN, R. D., STREETT, C. L. & CHANG, C.-L. 1993 Spatial direct numerical simulation of boundary-layer transition mechanisms: validation of PSE theory. *Theoret. Comput. Fluid Dyn.* **4**, 171–288.

KACHANOV, YU. S. & LEVCHENKO, V. YA. 1977 Nonlinear development of a wave in a boundary layer. *Fluid Dyn.* **12**, 383.

KACHANOV, YU. S. & LEVCHENKO, V. YA. 1984 The resonant interaction of disturbances at laminar–turbulent transition in a boundary layer. *J. Fluid Mech.* **138**, 209.

KENDALL, J. M. 1967 Supersonic layer stability experiments. In *Boundary Layer Transition Study Group Meeting* (ed. W. D. McCauley), *Rep.* BSD-TR-67-213, vol. II, US Air Force, pp. 10-1-10-8 (available from DTIC as AD 820 364).

KENDALL, J. M. 1975 Wind tunnel experiments relating to supersonic and hypersonic boundary-layer transition. *AIAA J.* **13**, 290–299.

KLEBANOFF, P. S. & TIDSTROM, K. D. 1959 Evolution of amplified waves leading to transition in a boundary layer with zero pressure gradient. *NASA Tech. Note* D195.

KLEBANOFF, P. S., TIDSTROM, K. D. & SARGENT, L. M. 1962 The three-dimensional nature of boundary layer instability. *J. Fluid Mech.* **12**, 1.

KLEISER, L. & ZANG, T. A. 1991 Numerical simulation of transition in wall-bounded shear flows. *Ann. Rev. Fluid Mech.* **23**, 495–537.

KOSINOV, A. D., MASLOV, A. A. & SHEVELKOV, S. G. 1990 Experiments on the stability of supersonic laminar boundary layers. *J. Fluid Mech.* **219**, 621–633.

LAUFER, J. & VREBALOVICH, T. 1960 Stability and transition of a supersonic laminar boundary layer on an insulated flat plate. *J. Fluid Mech.* **9**, 257–299.

LI, F. & MALIK, M. R. 1992 Step-size limitation for marching solution using PSE. Presented at the *45th Annual Meeting of the APS, Division of Fluid Dynamics, Tallahassee, Florida, Nov. 22–24.*

MACK, L. M. 1969 Boundary-layer stability theory. *Document* 900-277, *Rev.* A. JPL, Pasadena.

MALIK, M. R. 1990 Numerical methods for hypersonic boundary layer stability. *J. Comput. Phys.* **86**, 376–413.

MALIK, M. R., CHUANG, S. & HUSSAINI, M. Y. 1982 Accurate numerical solution of compressible, linear stability equations. *Z. Angew. Math. Mech.* **33**, 189.

MALIK, M. R., LI, F. & CHANG, C.-L. 1994 Crossflow disturbances in 3D boundary-layers: nonlinear development, wave interaction and secondary instability. *J. Fluid Mech.* **268**, 1–36.

MASAD, J. A. & NAYFEH, A. H. 1991 Effect of heat transfer on the subharmonic instability of compressible boundary layers. *Phys Fluids* A **3**, 2148–2163.

MORKOVIN, M. V. 1969 Critical evaluation of transition from laminar to turbulent shear layer with emphasis on hypersonically travelling bodies. *AFFDL-TR*-68-149 (available as NTIS AS-686178).

NG, L. & ERLEBACHER, G. 1992 Secondary instabilities in compressible boundary layers. *Phys. Fluids* A **4**, 710–726.

PATE, S. R. 1971 Measurements and correlations of transition Reynolds numbers on sharp slender cones at high speeds. *AIAA J.* **9**, 1082–1090.

PRUETT, C. D. & CHANG, C.-L. 1993 A comparison of PSE and DNS for high-speed boundary-layer flows. *ASME Fluids Engineering Conf., Washington, D.C., June 21–24, 1993.*

PRUETT, C. D. & ZANG, T. A. 1992 Direct numerical simulation of laminar breakdown in high-speed, axisymmetric boundary layers. *Theoret. Comput. Fluid Dyn.* **3**, 345–367.

SARIC, W. S. & THOMAS, A. S. W. 1984 Forced and unforced subharmonic resonance in boundary-layer transition. *AIAA paper* 84-0007.

SCHMID, P. J. & HENNINGSON, D. S. 1992 A new mechanism for rapid transition involving a pair of oblique waves. *Phys. Fluids* A **4**, 1986–1989.

SPALART, P. R. & YANG, K.-S. 1987 Numerical study of ribbon-induced transition in Blasius flow. *J. Fluid Mech.* **178**, 345–365.

STETSON, K. F. & KIMMEL, R. L. 1992 On hypersonic boundary-layer stability. *AIAA Paper* 92-0737.

THUMM, A., WOLZ, W. & FASEL, H. 1989 Numerical simulation of spatially growing three-dimensional disturbance waves in compressible boundary layers. In *Proc. Third IU-TAM Symp. on Laminar–Turbulent Transition, Toulouse, France, Sept. 11–15.*

VIGNERON, Y. C., RAKICH, J. V. & TANNEHILL, J. C. 1978 Calculation of supersonic viscous flow over delta wings with sharp subsonic leading edges. *AIAA Paper* 78-1337.

ZANG, T. A. & HUSSAINI, M. Y. 1990 Multiple paths to subharmonic laminar breakdown in a boundary layer. *Phys. Rev. Lett.* **64**, 641–644.